Detailed multi-insturment analysis of the very high γ-ray emission in the region of HESS J1813-178

Master's Thesis in Physics

Presented by

Tina Wach

Date: March 28, 2022

Erlangen Center for Astroparticle Physics
Friedrich-Alexander Universität Erlangen-Nürnberg
Germany

Supervisor: Prof. Dr. Stefan Funk

Abstract

HESS J1813-178 is one of the brightest and most compact objects detected by the HESS Galactic Plane Survey. Within the extent of the TeV emission lies a young Supernova Remnant G12.8-0.02 and a pulsar wind nebula driven by a pulsar with the second highest spin-down luminosity of known pulsars in the Galaxy, PSR J1813-1749. The origin of the TeV emission is still not clear. Because of the young age of the system, the pulsar wind nebula and the Supernova Remnant overlap and present a good opportunity to examine how the interactions between these two components influence the acceleration of particles in the system. In previous analyses, a discrepancy in extension has been observed between a point-like component seen in TeV γ-rays measured by H.E.S.S and a extended component in GeV γ-ray observations from the Fermi-LAT satellite. In this thesis, 3 dimensional map-based analysis with gammapy is performed to do a morphological and spectral analysis of this region in GeV and TeV energy ranges, as well as a joint-analysis of both datasets. A new significant extended emission component in the TeV energy range, with a morphology close to the GeV energy range, is detected. This analysis allows a consistent description and a smooth energy spectrum of the region across five decades of energy. While the question of the origin of the very high γ-ray emission from HESS J1813-178 could not be answered yet, this work provides insight into the physical processes present in the region.

Contents

1 Introduction

In 1912, the Astrian physicist Victor Hess started an experimental study concerning the measurable radiation on earth. The common believe at this time was that the origin of the observed radiation was γ-radiation from radioactive substances in the earth's crust. Following this thesis, he used a hot air ballon to measure the radiation at different altitudes up to $\approx 5\,\text{km}$ above the ground level. He expected to observe an linear decrease of the radiation with altitude.
Up to an altitude of $1\,\text{km}$, the experimental data proved the theory to be valid. Starting at roughly $3\,\text{km}$ height, he observed increasing radiation with increasing altitude. From these observation Victor Hess concluded the existence of a highly penetrating radiation component which originates beyond the earth's atmosphere. He also concludes that this radiation is not related to the Sun, as no fluctuations could be observed during an solar eclipse. [1]

In the years following the discovery by Victor Hess, many experiments probed the nature of this cosmic radiation and, with the help of many different experiments, an all particle spectrum was derived (figure 1.1). This radiation consists mostly of protons and heavier nuclei, the exact composition is energy dependent. It covers over 10 orders of magnitude in energy and shows two distinctive features. A spectral break at $\approx 10^{16}\,\text{eV}$, called the 'knee', as well as a change ins spectral slope at $\approx 10^{19}\,\text{eV}$, referred to as the 'ankle'. It is believed that galactic sources, such as pulsars or supernovae are directly responsible for the cosmic rays below the knee. At energies higher than $\approx 10^{15}$, the particles can no longer be confined by the magnetic fields of these objects and stream away from the sources. The origin of the radiation measured above the ankle is believed to be extragalactic, the ankle is interpreted as a result of energy loss of protons by scattering of Cosmic Microwave Background (CMB) photons. [2] The last distinctive feature that can be observed in the all particle spectrum is the Greisen-Zatsepin-Kuzmin (GZK) cut-off at $\approx 5 \cdot 10^{19}\,\text{eV}$. This cut-off represents the maximum energy that protons can reach due to energy loss of interactions with CMB photons [3], [4]. Only heavier nuclei can reach higher energies. All further spectral changes between the knee and the ankle are interpreted as changes in the underlying acceleration mechanism of the cosmic ray particles.

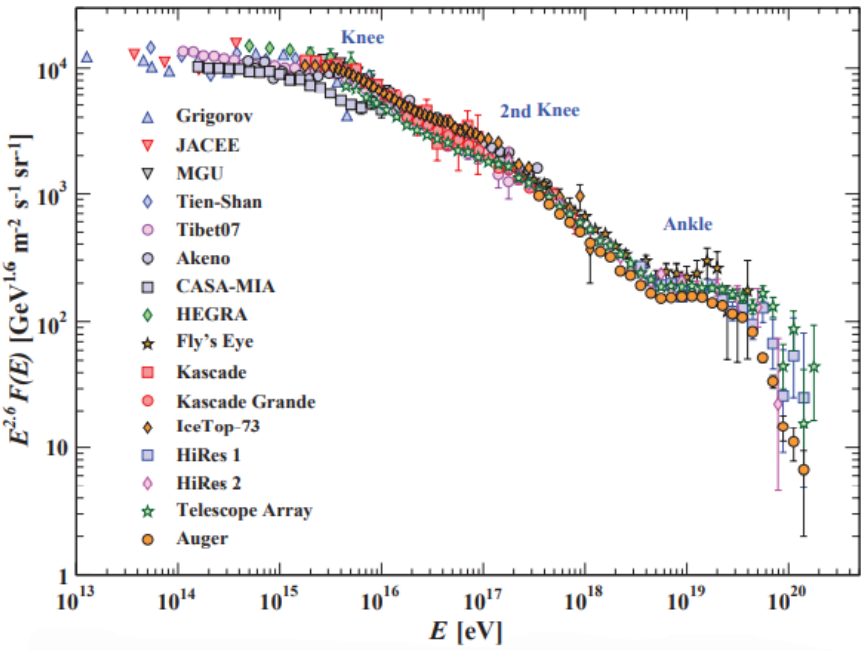

Figure 1.1: The all particle cosmic ray spectrum measured by air shower experiments. For better visibility, the y-axis was multiplied by $E^2.6$. [?]

2 Production mechanisms of high energy γ-rays in astrophysical sources

The acceleration of cosmic ray particles happens through different processes. The particles can be accelerated in a continuous way by an ordered field, this acceleration is labeled as inductive acceleration. Diffusive acceleration happens when the particle is accelerated in bursts in regions with high magnetic field intensity. Another acceleration mechanism that can be observed is Fermi acceleration, where the charged particle gains energy through the repeated passing of a shock front. [5]

2.1 Leptonic interactions

An example of an astrophysical source that produces emission mostly through leptonic channels are pulsars and pulsar wind nebulae. Electrons and Positrons travel along the magnetic field lines , with a component of the velocity perpendicular to the magnetic field lines, which accelerates the particle and induces an electromagnetic radiation. These synchrotron emitting electrons can also scatter of the cosmic microwave background or other photon fields, increasing the energy of these photons up to more than 100 TeV, through inverse Compton scattering.

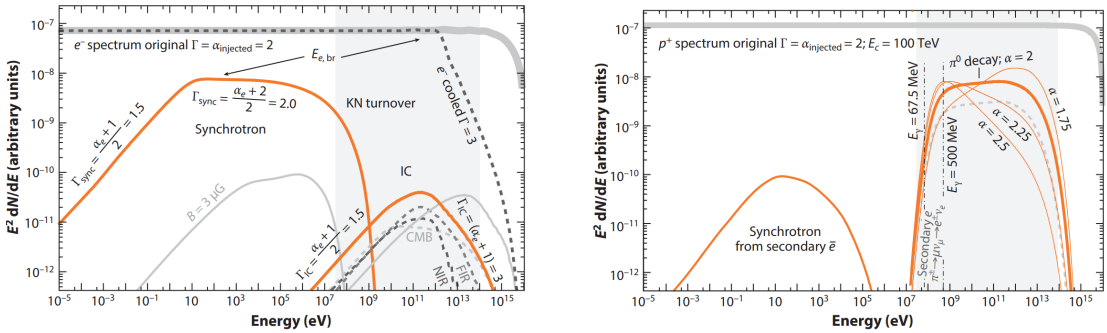

Figure 2.1: The γ-ray spectrum from synchnrotron and inverse Compton scattering on the left. On the right, the γ-ray emission produced by inelastic collisions of high energy protons with interstellar material.[6]

The characteristic shape of photon emission from such a leptonic accelerator can be seen in figure 2.1a.

2.2 Hadronic interactions

Hadronic interactions can be observed in Supernovae and Supernova remnants. High energy protons interact with matter close to the acceleration region and produce pions. These pions then decay into photons, leptons and the corresponding neutrinos. The shape of such a hadronic accelerator can be seen in figure 2.1b.

3 Evolution of Pulsar Wind Nebulae

3.1 Core collapse Supernova and their end products

The energy output of a star is produced by nuclear fusion. In the beginning of the evolution of a star, hydrogen is fused into helium. During this process the radiation pressure inside this iron core counters the gravitation. After most of the hydrogen is used up, the star cools and contracts, which increases the pressure inside the system and the fusion of helium into Carbon is started. This cycle continues until the burning of Iron. At this point the reactions become endothermic and the fusion stops. The Fermi energy of the electrons increases until inverse beta decay is energetically convenient, producing neutrons and neutrinos. The radiation pressure drops and the core collapses inward. This collapse is abruptly slowed down by the degeneracy pressure of the neutron gas countering the gravitational force.
This abrupt slowing of the collapse and the energy deposited in the neutrinos drives a supernova explosion. This outward moving shock wave then propagates into the interstellar medium with almost constant velocity. Due to the heating of the ISM a big shell of hot plasma is produced. This evolutionary phase is called the free expansion phase. After a few hundred years the shock wave has swept up a significant mass and the energy is divided into kinetic and ther-

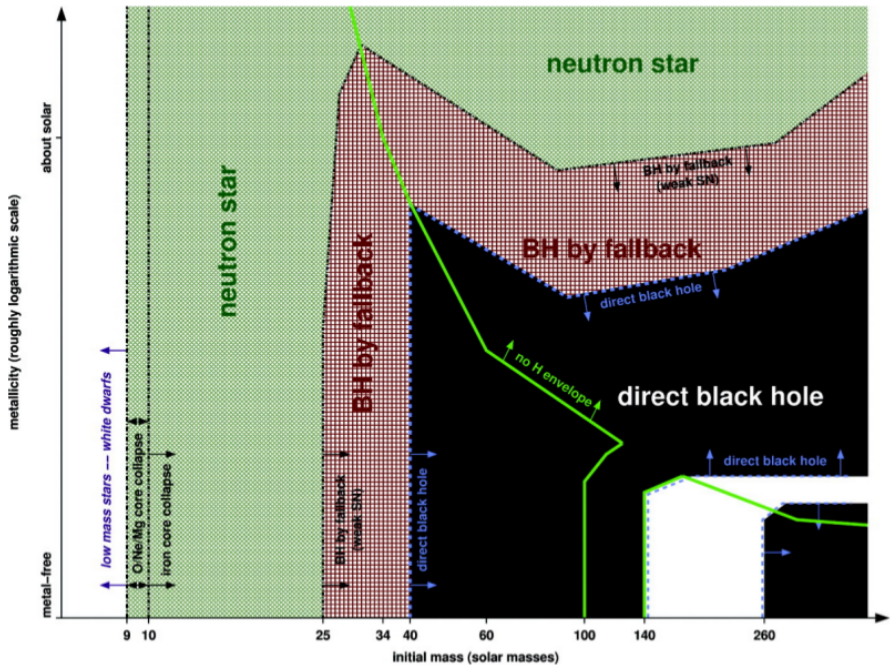

Figure 3.1: The different final states after collapse of a massive star, depending on its initial mass and metallicity. [7]

mal energy and a reverse shock forms at the interaction region of the ISM and the SNR. The forward shock heats the ambient gas and ejecta are decelerated, compressed and heated in the reverse shock. Only the material between the two shock fronts is hot. The SNR is now in the "Sedov-Taylor" phase. The reverse shock moves inward until it reaches the center of the SNR, which is therefore filled with shocked-heated ejecta.
The further evolution of the collapsing core depends on the initial mass and the metallicity of the star (figure 3.1). For stars with an Mass higher than $25\,M_\odot$ and a metallicity below the metallicity of the sun, the degeneracy pressure is not sufficient to stop the collapse and a stellar mass black hole is created.
In case of an initial mass below $25\,M_\odot$, the degenerate neutron gas is able to counter the gravitational force and the star becomes stable again. These neutron stars are mostly composed of neutrons, with a surface comprised of charged particles such as electrons or ions.

During the collapse, the Magnetic flux ($\Phi_B = B/R^2$) and the angular momentum ($L \propto \omega \propto R^{-2}$) of the massive star is conserved, but the size of the object decreases dramatically, therefore the rotation period of the star reduces drastically from days to minutes or seconds and the rotation speed ω and magnetic field strength increase. [8]

3.2 Pulsars

Pulsars are rapidly rotating neutron stars. The pulsed radiation that identifies this object, is created due to misaligned magnetic and rotational axis. The rotation of the magnetized neutron

star induces an electric field, which accretes particles from the stars surface. These particles are mostly confined in the magnetosphere of the star, but can escape over open magnetic field lines at the magnetic poles (figure 3.2). They travel along the magnetic field lines producing

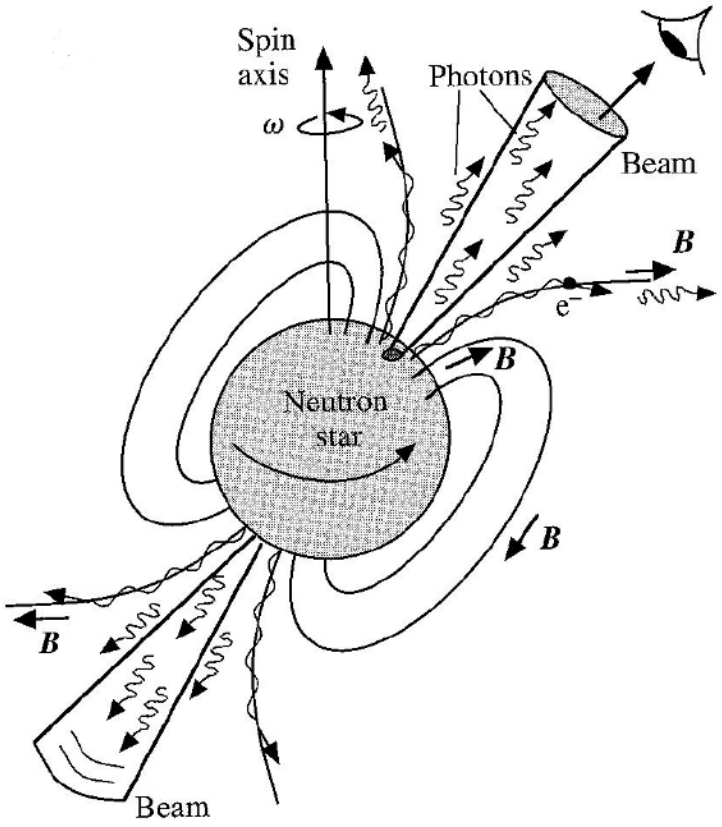

Figure 3.2: A schematic of a highly magnetized neutron star. The synchrotron emission can be observed once every spin period. Image credit: lecture extreme astrophysics, chapter 03 slide 30

synchrotron emission, which can then produce high energy secondary particles. This leads to beams of electromagnetic radiation along the magnetic field lines. Because of the misaligned axis, these radiation beams point towards the observer once each spin period and the pulsed emission over a big energy range can be observed. [8]

The rate at which rotational kinetic energy is dissipated, is called spin down luminosity $\dot{\mathrm{E}}$:

$$\dot{\mathrm{E}} = -\frac{d\mathrm{E}_{\mathrm{rot}}}{d\mathrm{t}} = 4\pi^2 \mathrm{I} \cdot \frac{\dot{\mathrm{P}}}{\mathrm{P}^3} \tag{1}$$

with the spin period P, I the moment of inertia of the neutron star and $\mathrm{E}_{\mathrm{rot}}$ the rotational energy. Typically it is assumed that $\mathrm{I} = 10^{45}\,\mathrm{g/cm}^2$.

After a pulsar spun down from the initial spin period P_0, in a manner that ensures $2\pi/\dot{P} = -k(2\pi/P)^n$, the true age τ can be calculated using the braking index n:

$$\tau = \frac{P}{(n-1)\dot{P}}\left[1 - \left(\frac{P_0}{P}\right)^{n-1}\right] \tag{2}$$

The braking index has only been measured for few Pulsars, therefore it is generally assumed that $n = 3$. [9]

3.3 Pulsar Wind Nebula [9] [10], [9], [11]

After the formation of the pulsar, charged particles swept up of the surface of the star can escape the light cylinder either near the polar caps or in the outer regions. These escaping particles (mainly ultrarelativistic electrons (e^-) and positrons (e^+)) form a termination shock in the ISM surrounding the pulsar, where the forward shock of the supernova has reduced the density of the ISM. The particles emitted from the pulsar wind are accelerated at the wind termination shock during each crossing of the termination shock front and form a nebula (also called plerion) around the pulsar. If this state is observed, a young pulsar centered at a reasonably symmetric pulsar wind nebula can be seen (figure 3.3).

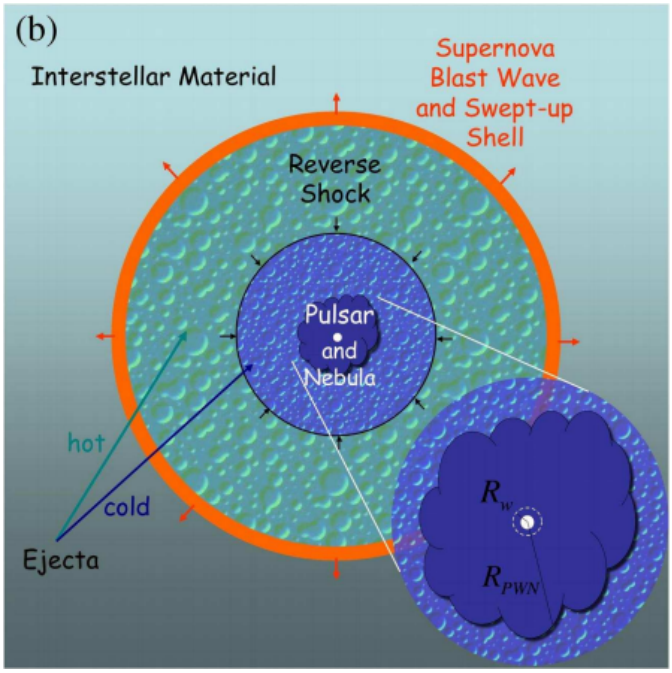

Figure 3.3: Schematic of the evolution of a SNR and the contained PWN. The rotational energy of the pulsar powers an expanding nebula that at one point meets the inward moving reverse shock of the supernova, which causes oscillations of expansion and compression in the PWN. [9]

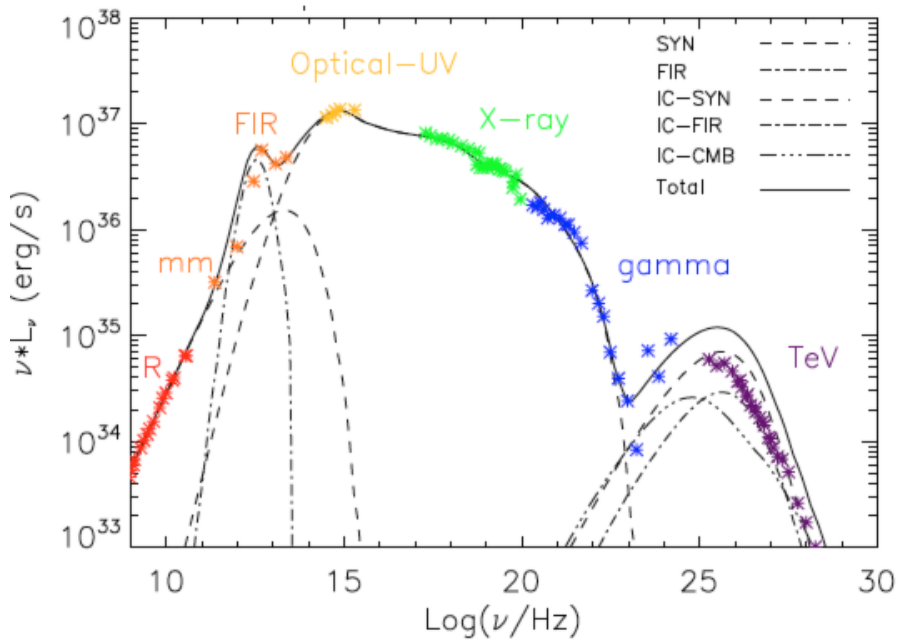

Figure 3.4: Spectrum of the Crab Nebula. [12]

The nebula is further expanding until the supernova remnant transitions into the Sedov-Taylor phase and the reverse shock travels back inwards and meets the nebula. The expansion of the supernova shock front depends highly on the density of the surrounding interstellar medium. Therefore it is possible that the shock extends further in one direction, creating an asymmetric shock front. This also results in an asymmetric reverse shock, which reaches the pulsar wind nebula at different times in different positions, causing a distortion in the spherical nebula. While it is compressed, the density in the pulsar wind nebula is increased and the pressure surpasses that in the reverse shock. This leads to a rapid expansion and decrease in the pressure. The system starts to oscillate and the process is repeated several times until the reverse shock dissipates and the pulsar wind nebula continues to grow around the current position of the pulsar. Additionally to the distortion through the reverse shock, the pulsar continues to travel with the drift velocity it acquired during birth, therefore adding to the asymmetry in the observed nebula. An example of a typical spectrum observed from an pulsar wind nebula can be seen in figure 3.4. At higher energies the emission caused by synchrotron radiation of the ultrarelativistic electrons wears off and the dominant emission mechanism becomes inverse compton scattering of the charged particles with photons of the cosmic microwave background.

After the pulsar has moved considerably from its birth position and the reverse shock of the supernova is dissipated, the nebula does no longer have a source injecting particles. The pulsar has created a new nebula around the current position and the particles in the relic pulsar wind nebula start to cool. The energy drops below the threshold for synchrotron emission that can

be observed in x-ray energies. The relic nebula is no longer prominent in x-ray energies. As the energy threshold for Inverse Compton scattering is lower than the one for synchrotron emission, the nebula is still visible and growing in the TeV energy range after the synchrotron emission has broken off. This leads to a large, distorted nebula with a offset from its pulsar. When the particles in the relic nebula cool further, the high energy emission also drops, leading to a softer spectrum and an energy dependent morphology of older pulsar wind nebulae.

4 HESS J1813-178

The source HESS J1813-178 was first detected during a survey of the inner part of the Galactic plane with the High Energy Stereoscopic System in 2005. HESS J1813-178 was detected with a significance level of $15.3\,\sigma$ at a position of 273.40° in galactic longitude and -17.84° in galactic latitude. The spectral index and flux derived in this analysis are $\Gamma = 2.09 \pm 0.08^\circ$ and Flux $= (14.2 \pm 1.1)10^{-12}\mathrm{cm}^{-2}\mathrm{s}^{-1}$ above 200 GeV. The detected source has an extension of $\sigma = 0.036 \pm 0.006$ degree, only slightly extended with respect to the point-spread function of HESS. The galactic plane survey also reports the hint of an extended emission at the position of HESS J1813-178, which was observed with a significance of below $5\,\sigma$, and therefore discarded. [13]

For source identification, the multiwavelength context is crucial. To firmly identify a counterpart to the gamma-ray emission detected in the galactic plane survey it needs spatial association as well as a consistent picture over a broad range of frequencies and a viable gamma-ray emission mechanism.
In the GeV to TeV range, the properties of HESS J1813-178 found during the galactic plane survey were soon after confirmed by the MAGIC Cherenkov telescope. [19]
Spatial coincidence for the γ-ray source HESS J1813-178 can be observed with the X-ray source AX J1813-178 detected by the ASCA observatory in the energy band of $2 - 10$ keV and also with the unresolved hard X-ray source IGR J1813-1751 detected by the INTEGRAL satellite in the $20 - 100$ keV energy range.
This region surrounding HESS J1813-178 was also observed by the Very Large Array in the 20 cm and 90 cm band. This observation lead to the discovery of a faint non-thermal radio source (G12.82-0.02), which was confirmed using the Spitzer Space telescope. The observed spectrum, morphology and absence of dust emission identifies this object as a young shell-like supernovae remnant. Additionally, another faint radio source W33 is detected in the projected vicinity to HESS J1813. The ultracompact H II star forming region extends over $15'$ with a distance of $10'$ from HESS J1813-178. The spatial coincidence of the TeV emission and the radio and X-ray sources can be seen in figure 4.1, where the white contours depicts the ASCA contour and black the 20 cm radio emission observed by VLA. The position of W33 is also indicated. [13]
From these observations it was unclear whether the emission observed in X-ray and γ-ray energies has its origin in the shell of the supernova remnant, a PWN embedded in the shell of the SNR or the interaction of accelerated hadrons with the dense molecular clouds present in W33.

To identify the unknown γ-ray source, Funk et. al. (2007 [14]) used data acquired with the satellite XMM-Newton. Due to a high angular resolution and high sensitivity, this satellite is well suited for identification of a X-ray counterpart to the high energy emission. This observation yielded a compact X-ray source with an extended tail towards the north-west with a morphology similar to the HESS source. The detection of the shell-like radio emission observed by VLA, paired with a compact core X-ray emission, detected by XMM-Newton indicates that

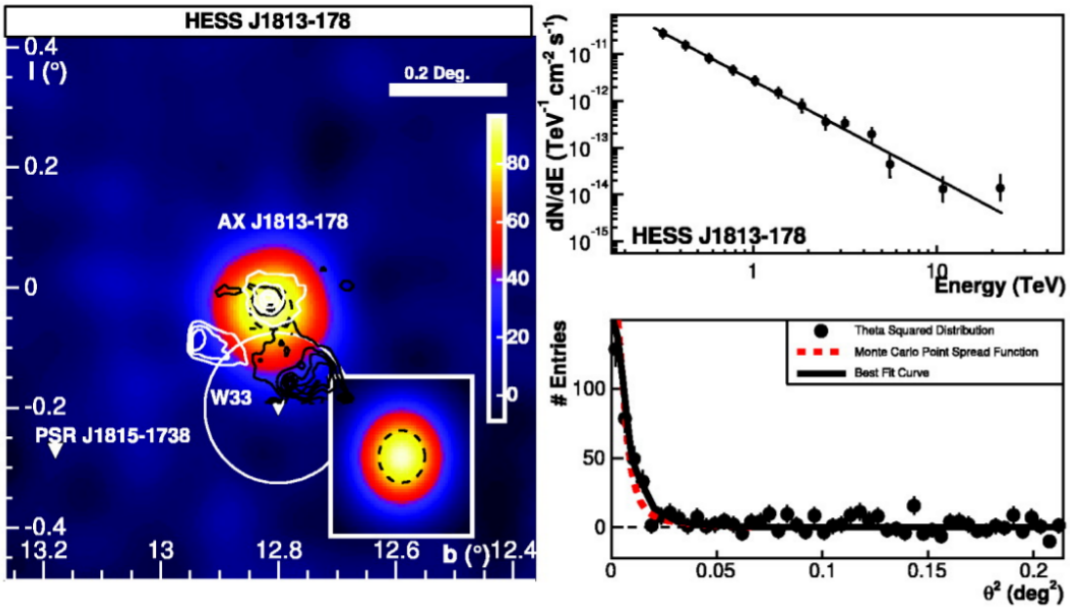

Figure 4.1: Left: Excess map of the region surrounding HESS J1813 acquired with HESS. The white contours show the corresponding x-ray emission in the $0.7 - 10$ keV range, while the black contours show the radio emission. Right: The spectrum and theta-squared dependence of HESS J1813 derived in the galactic plane survey. [13]

the origin of the emission is a young, energetic pulsar powering a pulsar wind nebulae, but a hadronic origin can not be rejected.
The physical model corresponding to a leptonic origin of the observed TeV emission can be seen in the upper plot in figure 4.2. The dashed line represent a synchrotron/IC scattering model with a low energy break or cutoff. The solid line represents a leptonic model with a strong contribution of scattering by infrared or optical radiation fields. Even though the energy density needed for this model exceeds the expected energy density by a factor of 10^3, the model is still valid because of the close proximity to W33. Both models imply that HESS J1813 is a leptonic PeVatron, accelerating electrons to energies above 1 PeV. There has been no indication for such high energy electrons in previous analysis of HESS J1813-178.
Additionally to the two plerionic creation scenarios above, is a origin of the γ-rays in the SNR shell. The extension of the TeV emission is consistent with the extension of the shell-type radio source. Funk et. al. reports two possible scenarios in which the emission originates in the SNR shell. The first is an inverse Compton emission of the same electrons producing the radio shell (solid line in the lower plot in figure 4.2).

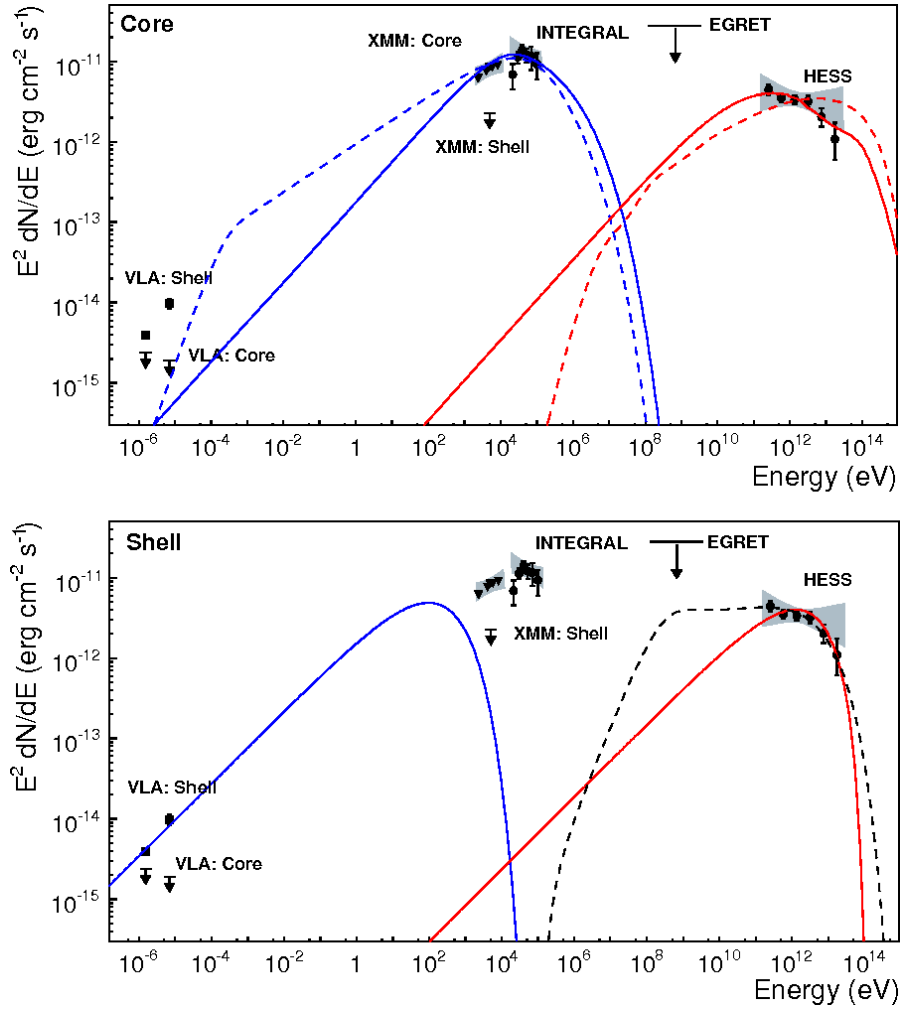

Figure 4.2: A combined spectrum from the data taken with VLA, the INTEGRAL satellite, XMM-Newton, EGRET and HESS. The top plot shows the physical models in case of a origin from synchrotron/inverse Compton scattering of electrons in a PWN. The bottom plot shows the physical model in case of a photon origin in the SNR shell. The differences between dashed and solid lines originate from different model parameters. [14]

The second scenario (dashed line) is a hadronic emission of the γ-rays and involves the acceleration of protons in the SNR shell, producing neutral pions, which then decay. The maximum energy in both of these scenarios is below 100 TeV.

The theory of a plerionic origin of the X-ray and γ-ray emission from HESS J1813 was further backed by the discovery of the high energy X-ray pulsar PSR J1813-1749 (Gotthelf et. al., 2009, [15]) using XMM-Newton. The pulse period of PSR J1813-1749 is 44.7 ms. With a spin-down

luminosity of $\dot{E} = 5.6 \cdot 10^{37}$ erg/s, PSR J1813-1749 has the second highest spin-down luminosity observed in the galaxy.
Camilo et al. [52] estimates the tangential velocity of the pulsar to 1490 km/s, assuming a distance of 4.8 kpc and even larger for higher distances. Such a high velocity would be larger than any velocity measured for a neutron star. If this value is correct, the positional coincidence of the pulsar and the SNR G12.82-0.02 implies that the system has a very young age of approximately 300 yr, instead of the characteristic age of $\tau = 5600$ yr. The young age could explain the positional coinicdence, but the spectral energy distribution observed in the TeV energy range shows characteristics of an evolved system. Because this result invites scepticism, the radio proper motion was recalculated using high-angular-resolution data taken by the VLA over 12 years. Dzib et al. [56] conclude that PSR J1813-1749 has a transverse speed of roughly 400 km/s and estimate the age to ≈ 1350 yrs, being in agreement with the TeV emission and the positional coincidence with the SNR.
In previous studies of the region, an association between the stellar cluster Cl 1813-178 located in the starforming region W33 and the progenitor of the supernova remnant G12.82-0.02 has been made [54], [55]. More recent studies show, that this associations might not be correct. The absorbing column densities to the pulsar and the cluster are discrepant. While the X-ray absorption to Cl 1813-178 is estimated to $N_H = 2 \cdot 10^{22}$ cm^{-2}, the value derived for G12.82-0.02 is $N_H = (10 \pm 1) \cdot 10^{22}$ cm^{-2}. The distance to Cl 1813-178 is estimated to 4.8 kpc, while the meansured column density for the SNR is consistent with a distance between $5 - 12$ kpc. The dispersion measure of 1087 pc/cm^3, indicating a distance between 6.2 and 12 kpc, is consistent with this estimation. Further evidence for a this large distance to PSR J1813-1749 comes from the comparison with the X-ray absorption to a source that lies in a projected distance of 0.7° along the Galactic plane. The distance to this source was estimated to 7 ± 1 kpc. The observed column density to this source is less than one third of the denisty observed to the pulsar, therefore indicating an even larger distance. [52], [53] If this distance estimation of 6.2 to 12 kpc for PSR J1813-1749 is correct and the TeV source is associated to the pulsar, the distance between the cluster Cl 1813-178 and the TeV source HESS J1813-178 is large. Therefore an interaction of particles of the pulsar wind nebula with the molecular clouds in the cluster is very unlikely and would not produce high energy emission, as the particles from HESS J1813-178 would have lost a considerable amount of energy before interacting with the clouds. Considering this large distance, the assumption that the emission from HESS J1813-178 could result from the interaction of high energy particles with molecular clouds present in the star-forming region W33 is wrong.

These findings and the high spin-down power of the PSR support the interpretation that the origin of the TeV emission observed by HESS is the pulsar wind nebula. This was further backed by Fang & Zang (2010, [16]) who also come to the conclusion that the VHE γ-rays are most likely produced by IC scattering of electrons inside the nebula. To come to this conclusion, they used an distance estimate of 4.7 kpc and an characteristic age of 1.2 kyr. Considering the new distance estimation, the results derived in this analysis are not reliable.

Another study of HESS J1813-178 in the GeV range was done by Miguel Araya (2018, [18]).

He used the observations by the Fermi Large Area Telescope in an energy range between $0.5 - 500\,\mathrm{GeV}$. This energy range was chosen as there was substantial soft emission below $500\,\mathrm{MeV}$ observed in the vicinity of the source, which could not be explained and complicated the analysis. They report considerable results in the LAT data after subtracting the point source hypothesis model found by HESS and XMM-Newton and propose an extended emission.
The best fit values of this analysis are a position of RA $= 273.292$, DEC $= -17.617$. The spectral index measured in this analysis ($\Gamma_{\mathrm{LAT}} = 2.07 \pm 0.09^{\circ}$) is compatible to the result found in the HESS Galatic Plane Survey [13] ($\Gamma_{\mathrm{LAT}} = 2.09 \pm 0.08^{\circ}$) and softer than the usual IC emission spectrum seen in PWN. In difference to the TeV emission measured by HESS, the GeV emission is extended with a radius of $0.6 \pm 0.06^{\circ}$. The hard spectral index of this extended emission is inconsistent with a leptonic origin in the PWN, therefore they suggest a hadronic accelerator as origin.

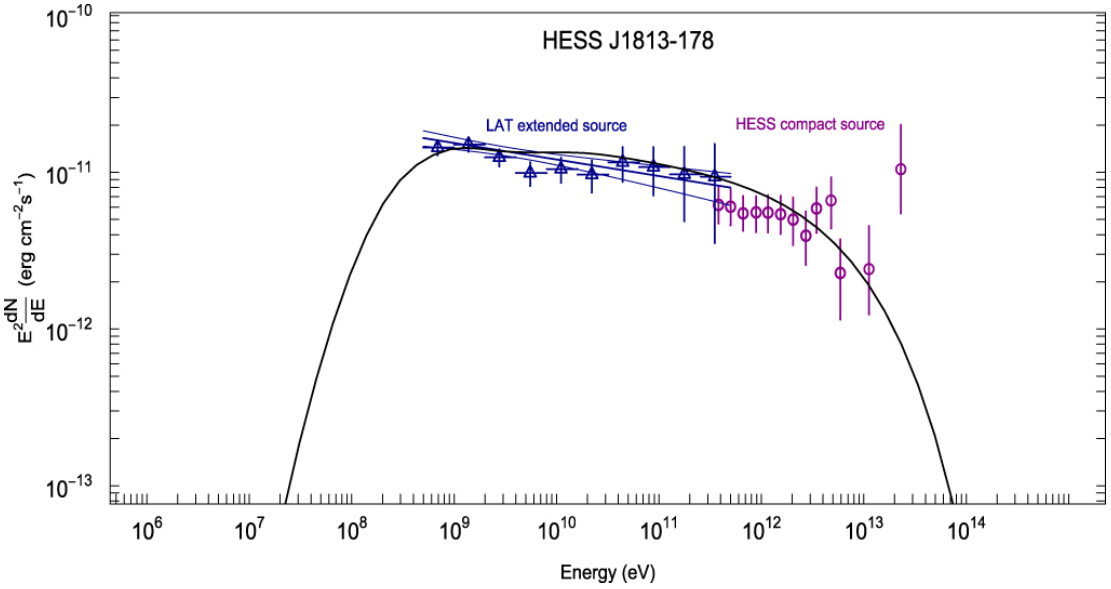

Figure 4.3: The hadronic model for the GeV emission coming from HESS J1813 applies well to the SED derived by Fermi-LAT. [18]

The physical model, as well as the SED for LAT and HESS can be seen in figure 4.3.
Considering that the extension of the GeV emission is bigger than the angular size of the SNR ($\approx 2.2'$), the accelerated particles would have to have escaped from the remnant. In case of a origin in W33, it could point towards a previously unknown component of star formation, as this behaviour was also observed in other star forming regions. Another scenario they conclude is a contribution of a number of SNR's close to HESS J1813. A possible plerionic origin can't be disregarded, as rapid electron diffusion from the pulsar wind nebula could also produce a spectrum with a hard photon index and lack of spectral curvature.
They also report a point-like structure at the position of the TeV peak, most likely related to the PWN. But this emission has a TS of below 25, therefore no detection can be claimed.

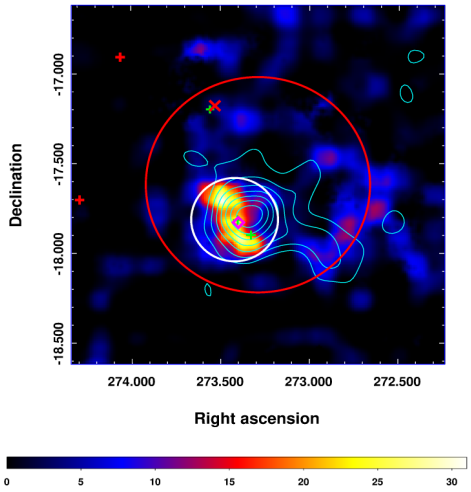

(a)

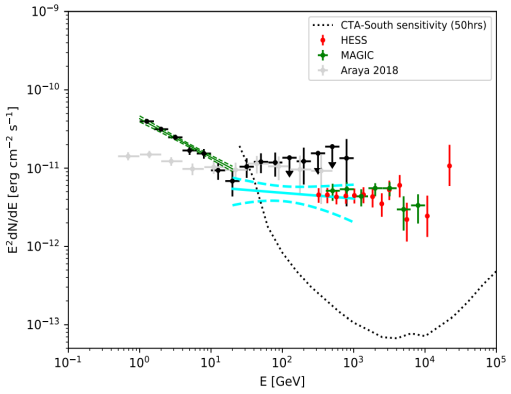

(b)

Figure 4.4: Left side: A TS map of the region surrounding HESS J1813. The magenta diamond marks the centroid position of the emission derived in the HESS analysis, the cyan contours are from the MAGIC analysis. The red plus marks 4FGL sources, while the green plus marks the position of SNR's in the vicinity. The morphology for the fit in the energy range of 1 GeV to 20 GeV is indicated in red, while the position of the best-fit value for the higher energy range is indicated by the white circle. Right: The spectral energy distribution of the Fermi-LAT data (black SED) compared to previous analysis and HESS data. [19]

The results from the data accumulated using the Fermi-LAT were then reanalyzed by Xin and Guo (2021, [19]). The SED of this analysis in comparison to the ones derived by Araya et al. [18] can be seen in the left plot in figure 4.4b. Because of the upturn in the spectrum, Xin and Guo divided the energy range into two parts, from 1 GeV to 20 GeV and from 20 GeV to 1 TeV. They report an extension of 0.56° and a rather soft spectrum ($\Gamma = 2.49$) in the lower energy range. The morphology in the lower energy range is consistent with the results derived by Araya et al. [18]. In the higher energy range, they report a spatial extension of 0.23° and a spectrum consistent with the one derived in the HESS analysis. The position and extension in respect to the HESS analysis can be seen in figure 4.4a.

As seen in many previous analysis of the source HESS J1813, the origin of the very high energy γ-rays is still not determined. None of the different scenarios of origin can be ruled out with the data accumulated in different energy ranges. Also the question remains why the source is extended in the GeV energy range and point-like in the TeV emission range. To shed further light into the behaviour and origin of this emission, further analysis of this region is necessary.

5 Detection of γ-rays

γ-ray detectors can be divided into two major categories. $\gamma-$rays can be detected from space, using telescopes mounted to satellites or via ground-based detectors. The detection via telescopes mounted to satellites brings the advantage of very low background, a bigger field of view and the ability to observe the whole sky. Ground-based detectors only have a limited field of view, a high angular resolution and the background is much higher than the signal. But due to the mass constraint of a satellite, a space based telescope can not acquire data in the TeV energy range, as the small detector area can not compensate the low γ-ray flux at high energies. In the following both methods will be discussed in regards to the Fermi-LAT and the H.E.S.S experiment.

5.1 Imaging Atmospheric Cherenkov Telescopes

The Imaging Atmospheric Cherenkov Telescopes (IACT's) are ground-based air Cerenkov detectors. For detection they use the Cherenkov light emitted by particles in a particle shower resulting from the interaction of a high energy γ-ray particle with the atmosphere.

5.1.1 Air shower development

Besides the γ-rays, also other particles, such as electrons, protons or heavier nuclei reach the atmosphere. These cosmic rays are much more abundant than the γ-rays. The atmosphere of the earth represents about 12 interaction lengths of target material for a high energy cosmic ray particle. The first interaction between the particle and a nuclei in the atmosphere happens at an altitude of roughly 20 km. The showers induced by this interaction can be distinguished into two categories. Hadronic showers and electromagnetic showers.

Electromagnetic showers are induced when the incoming cosmic ray is a γ-ray, an electron e^- or a positron e^+. They interact with the atmosphere via bremsstrahlung and pair production. Following a model from Heitler and Rossi, these processes alternate until a critical energy level $\mathrm{E_{crit}} \approx 84\,\mathrm{MeV}$ is reached. Below this energy threshold ionization dominates over Bremsstrahlung, ending the particle cascade. The particle cascade induced by a γ-ray is visualized on the left side in figure 5.1. These showers can be identified by their contributing particles, their depth depends logarithmically on the energy of the primary particle.

Hadronic showers are the result of a proton or heavier nuclei interacting with the atmosphere. This interaction mainly produces neutral- and charged pions. These pions interact via inelastic collisions or decay into $e^{\pm}$ or in the case of charged pions into muons ($\mu^{\pm}$) and neutrinos. The muons then also decay into electrons and create further electromagnetic sub-showers. Therefore a hadronic shower has different sub-showers with different components and a larger transverse momentum. The shape of such a shower can be seen in figure 5.1. These differences are used to distinguish between an air shower produced by a γ-ray or electron or one that has a hadron as primary particle.

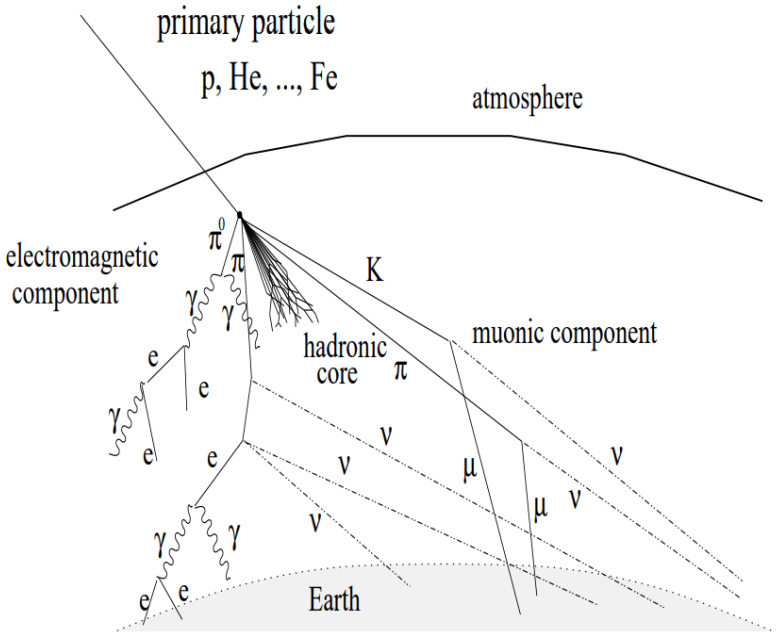

Figure 5.1: The development of an air shower induced by a particle interacting with the atmosphere. The shower can be divided into two different categories of sub-showers, the electromagnetic and the hadronic shower. The evolution of a hadronic shower is more complicated than an electromagnetic shower because of the strong interactions that take place [21]

5.1.2 Imaging Atmospheric Cherenkov Technique

If a particle travels through a medium with a speed higher than the speed of light in that medium, it polarizes the medium and electromagnetic waves are emitted along the track. This allows for a reproduction of particle track and energy. The photons are emitted in a cone that can be described by it's opening angle $\Theta = \arccos(c/vn)$, where v is the speed of the particle and n the refraction index of the medium. Following this formula, the Cherenkov light emission from a high energy γ-ray is characterized by a opening angle of $\Theta = 1^\circ$ increasing downwards and a radius of about $125\,\mathrm{m}$ at sea level.

The large opening angle of the Cherenkov cone results in a problem for γ-ray astronomy. The air showers are very extended in the direction of the primary photon, therefore the field of view of the Camera needs to be big. But the biggest challenge of γ-ray astronomy using Imaging Atmospheric Cherenkov Telescopes (IACTs) is a distinction of the signal from the background, consisting of photons produced in hadronic showers. Even in regions with a high signal, the background outnumbers the signal by a factor of 10^4.
To achive a background rejection, the differences in the development of showers induced by a cosmic ray hardron and a γ-ray, which results in a difference in the observed camera image, can be used. The signal observed from both cases can be seen in figure 5.2. Both incoming

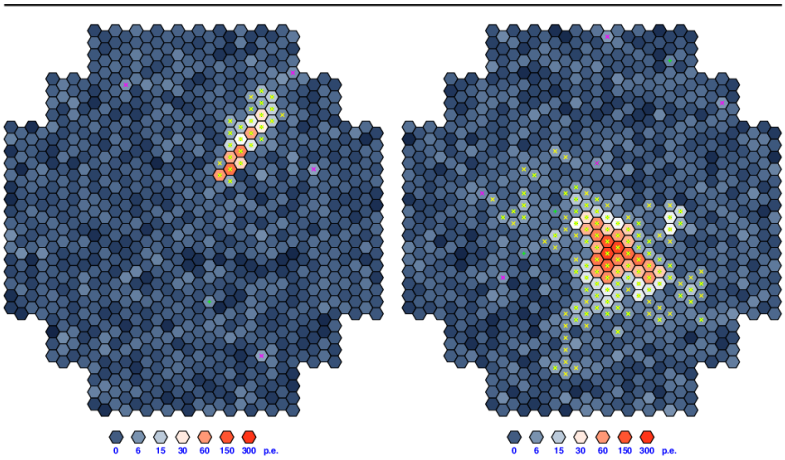

1.0 TeV gamma shower 2.6 TeV proton shower

Figure 5.2: The signal on the camera plane is different for air showers induced by γ-rays (left plane) and air showers induced by hadronic cosmic ray particles (right plane). [22]

particles result in an elliptical shape, but can be distinguished by the geometry of the ellipse. These parameters, length, width and angle and distance to the center position are called Hillas parameters. The signal observed in hadronic cosmic ray cascades is less elongated and appear larger, due to the large transverse momentum transfer in a hadronic interaction in the cascade. The background rejection using the Hillas Parameters produces good results, but it is only possible to obtain a projection of the air shower. To counteract this effect, and measure the full Cherenkov cone, multiple telescopes are placed in detector arrays. The images obtained from

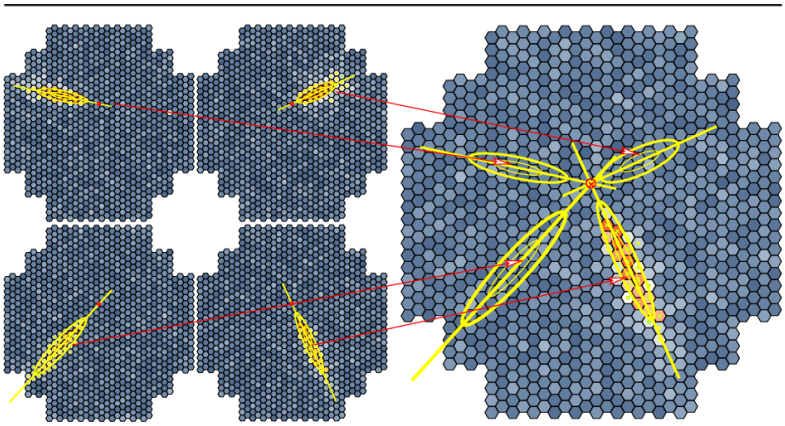

Figure 5.3: To achieve a reconstruction of the direction of the incoming γ-ray, telescopes are positioned in an array and the obtained images are combined. [22]

the respective cameras are then projected onto one camera and the intersection point of the major axis of the Hillas Parameters yields the shower direction (see figure 5.3). [22]

5.1.3 The H.E.S.S Experiment

The High Energy Stereoscopic System H.E.S.S. is an array consisting of Imaging Air Cherenkov Telescopes, and one of the main contributors to the advancement of ground-based gamma-ray astronomy. It is located in the Khomas Highland in Namibia, a site chosen because its high altitude, cloudless nights and low humidity, which provide good observation criteria. Additionally this location allows the telescope array to observe a large part of the sky (figure 5.4). This IACT array contributed highly to the understanding we have of the VHE gamma-ray sky,

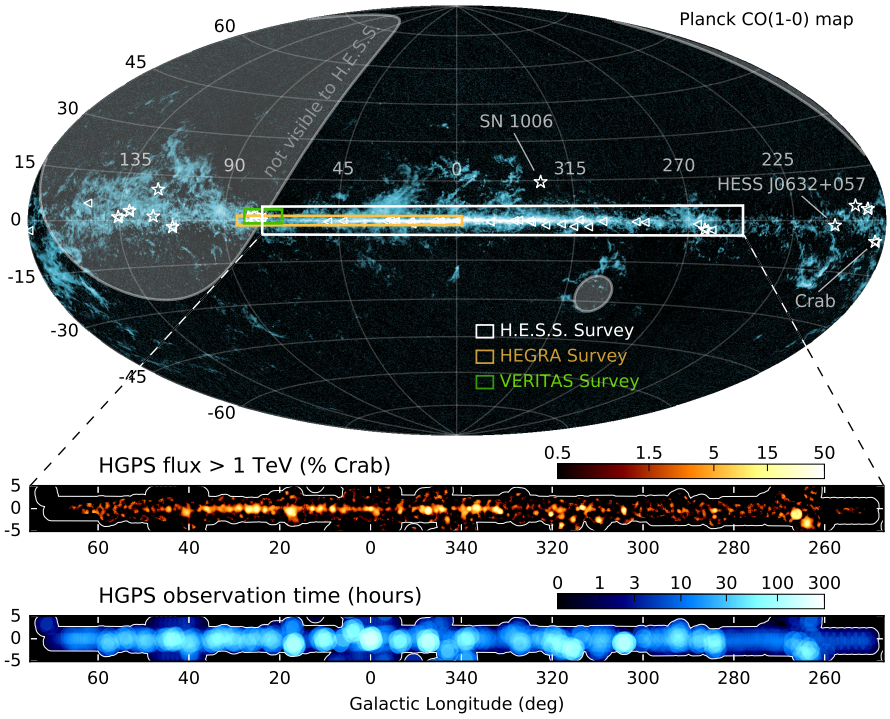

Figure 5.4: This all-sky map shows the distribution of carbon monoxide in the sky, as measured by the Plank satellite (Planck Collaboration X 2016). The sky region that is not visible to HESS is indicated as a gray area. The image was created during the HESS Galactic plane survey. [23]

as most of it's sources were discovered by the H.E.S.S experiment [28].
The first telescope of the array started observations in 2002. By December 2003 four identical telescopes, CT1 to CT4, were operating. The telescopes are positioned on a square of 120 m side length.
Each telescope has a reflector area of $107\,\mathrm{m}^2$ and reflectively of the mirrors of 80% to 90%. The cameras, which are mounted in the focal plane, consist of 960 photo-multiplier-tubes with an average of 15% quantum efficiency. The field of view of the cameras is 5° with a pixel size of 0.16°, which allows for a observation of extended sources. Considering the typical amount of Cherenkov photons at this altitude, the energy threshold of the H.E.S.S phase I constella-

tion is around 100 GeV. The upper energy limit of gamma-rays that can be detected with HESS is 100 TeV. Because of the combination of four spread out telescopes, as well as a good background rejection, HESS has an angular resolution of $< 0.1^{\circ}$. [26]
Due to aging of the photomultipliers and environmental influences of the reflectivity of the mirrors, the sensitivity of the telescopes has declined over time. [25] Therefore the cameras of the original array were replaced in 2016 to improve the performance and the following observations with this new cameras belong to the HESS-IU phase.

The IACT has a central trigger system, consisting of a camera trigger and a central trigger. The camera trigger can be divided into two separate trigger. One is a PMT threshold, rejecting short and weak signals from the night sky background and a second trigger on camera level ensuring that a signal is only detected if it is measured in at least three PMT's. The central trigger activates when a signal has been detected in at least two of the four telescopes within 80 ns. Through these trigger conditions the Night sky background rate can be significantly reduced and thus the IACT can operate with a lower dead-time. [27]

H.E.S.S phase II was initiated when the array was extended with a fifth telescope (CT5) in 2012. The reflective area of this fifth telescope is $\sim 600\,\mathrm{m}^2$, which reduces the energy threshold from 100 GeV with CT1-4, to tens of GeV. This telescope is located in the center of the square (figure 5.5)

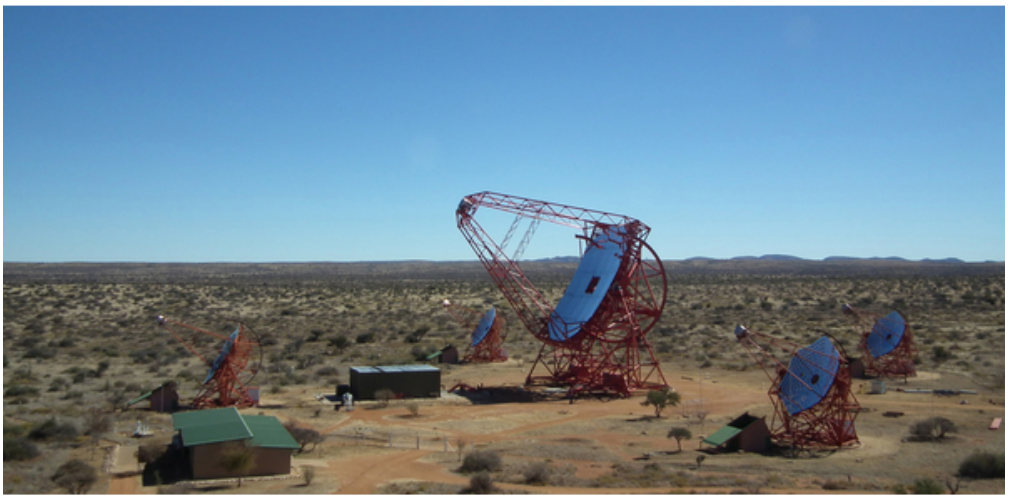

Figure 5.5: Layout of the IACT array HESS after adding a fifth telescope to lower the energy threshold. [24]

and has a diameter of 28 m. The addition of this telescope makes the H.E.S.S Telescope the first IACT array that operates different sized telescopes. [28]

5.2 The Fermi-LAT Satellite

The Fermi Gamma-ray Space Telescope has two instruments on board. The Gamma-Ray Burst Monitor and the Large Area Telescope (Fermi-LAT). With LAT being able to produce reliable data in an energy range of 20 MeV to 1 TeV, it is able to close the gap in energy range coverage between the satellite EGRET, actively measuring data between the years 1991 and 2000, with an energy range up to 30 GeV and H.E.S.S. Another improvement is the LAT's sensitivity, which stems from a large field of view, good background rejection, superior angular resolution and a large peak effective area. [29], [30] This allows the Telescope to observe the whole sky with a good accuracy due to a low dead time. A picture of the whole sky according to LAT can be

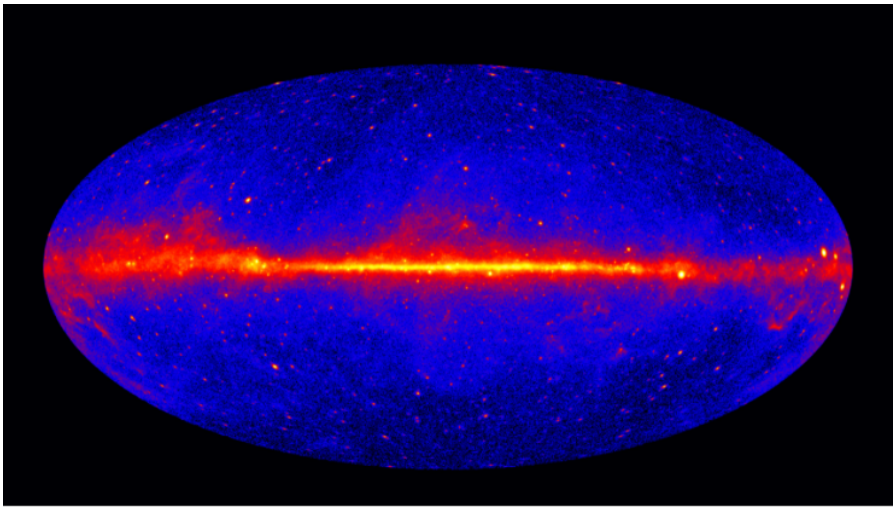

Figure 5.6: An all-sky image at energies greater than 1 GeV, after 60 months of data taking with the Fermi satellite. [32]

seen in figure 5.6.

The detection of the high energy γ-rays happens via pair-production into an electron-positron pair in a 4x4 array of identical towers. A schematic of the layout of one of these detection towers used by LAT can be seen in figure 5.7. The conversion takes place in 16 planes of tungsten foil, used because of it's high atomic number. Between these foils are silicon microstrip detectors that track the passage of the charged particles. With this information the directions of the incoming γ-rays can be reconstructed. Multiple scattering of the electrons and positrons through the detection layers results in a probability distribution of the reconstructed direction and thus limits the obtained resolution and defines the Point Spread Function (PSF).
Following this construction is a Ceasium iodide calorimeter, that tracks the development of the electromagnetic showers induced by the charged particles from the incident photon. Each calorimeter has 96 crystals, isolated from each other, with two photodiods at each end, which enables a good spatial resolution of the energy deposition. Another purpose of this calorimeter is rejection of the background consisting of hadronic cosmic rays, through tracking the development of the shower.

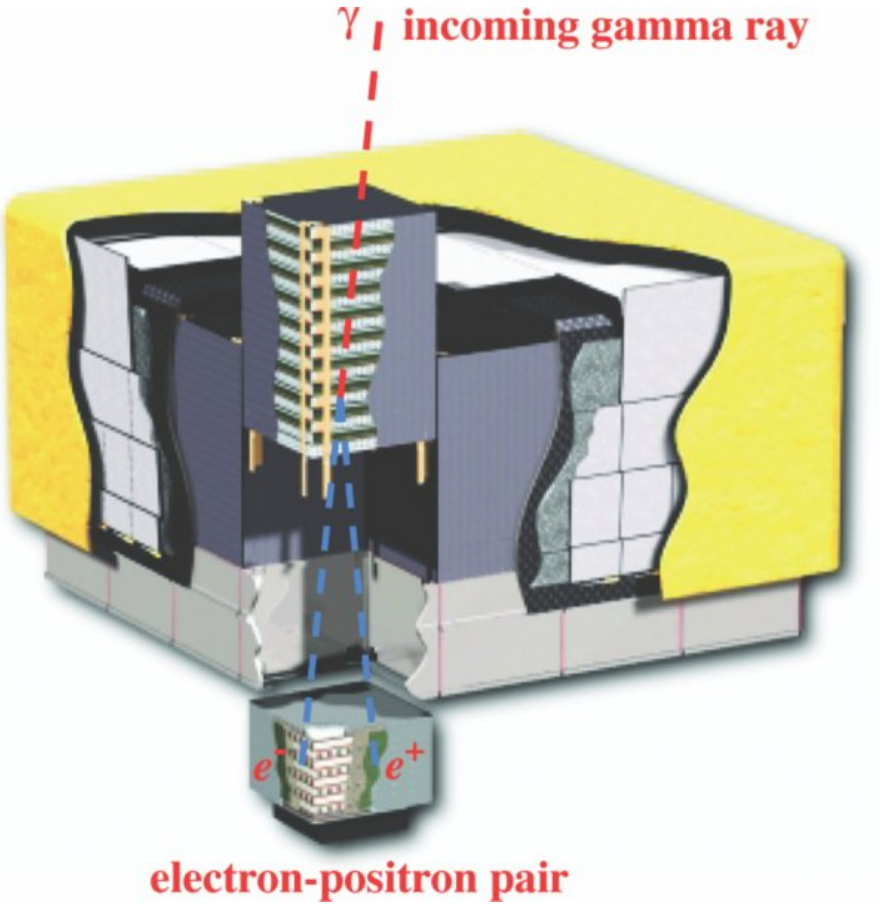

Figure 5.7: The Tracker consisting of interleaved foil and silicon detectors can be seen in the part that is coated in gray. The calorimeter located below this layer is indicated in the lower part of the sketch. The ADC coats the detection area and is depicted in white here. [31]

Even though the calorimeter also provides a way to separate hadronic and electromagnetic incidents, the main background rejection happens in the Anticoincidence detector (ADC). It consists of plastic scintillators with a detection efficiency of at least 0.9997 for single charged particles entering the field-of-view of the LAT. [31]

6 Data evaluation

6.1 Gammapy [38]

Gammapy is a open-source python-package, which is based on the existing scientific python packages scipy and numpy, as well as the python package for astrophysics, astropy. This package can be used to analyze data acquired with different IACT's, as well as Fermi-LAT and HAWC. In this analysis gammapy version 0.18.2 [38] is used.
Gammapy offers different analysis methods, the one used throughout this work is the three dimensional analysis, with one spectral dimension and two spatial dimensions.
The class WcsGeom is used to determine the field of view used in the analysis. It includes the number of pixel in each dimension, the binning and maximum and minimum value of the non-spatial axis as well as the center position of the dataset. This class is used to perform transformations between world coordinates and pixels and provides the geometry for the class MapDataset. The class contains the IRF's, as well as the counts and exposure cubes and safe energy and spatial masks defining which data can be used for the analysis.
After the data is processed, gammapy stores the results in the class WcsNDMap, which is based on a numpy array of map values.

The analysis is done via a binned maximum likelihood method. At first, the counts resulting from the models assigned to the MapDataset are predicted. For this step the geometry of the exposure map is used. The resulting map needs to have the same spatial dimension, but the energy binning can be choosen finer, which will increase the precision of the fit. After this step, the predicted counts map is combined with the energy dispersion matrix and the PSF and rescaled to the energy axis of the counts map. The residual emission of the dataset is then given as the difference between the predicted counts and the counts cube.

The two fitting methods available in gammapy are 'stacked' and 'joint'. In the stacked fit, the data of each individual run is summed and the likelihood value from this sum is calculated. In the joint fit, each run is fit individually and the final likelihood value is a product of the individual likelihood values. For very precise analysis a joint fit should be used, as the IRF's are also averaged in the stacked fit. But the joint fit is also computationally more expensive, therefore a semi-stacked fit is a good compromise.
The background model is already added during the stacking of the data and can be manipulated using the norm and tilt parameter. The emission predicted from this model is also saved in the predicted counts cube.

The test statistcs (TS-value) provides a measure of how accurate the model descibes the data. Using this TS-value, one can determine wether there are significant deviations between the predicted counts and the measured counts. To calculate this TS-value, the likelihood $\mathcal{L}$, needs to be calculated:

$$\mathcal{L} = \frac{(\mu_{\text{sig}} + \mu_{\text{bkg}})^{n_{\text{on}}}}{\mathrm{n}_{\text{on}}!} \exp\left(-(\mu_{\text{sig}} + \mu_{\text{bkg}})\right) \cdot \frac{(\mu_{\text{bkg}}/\alpha)^{n_{\text{off}}}}{\mathrm{n}_{\text{off}}!} \exp\left(-\mu_{\text{bkg}}/\alpha\right) \tag{3}$$

where μ_{sig} the number of predicated counts in the on region, μ_{bkg} the number of predicted background counts in the on region. The parameter n_{on}, n_{off} denotes the observed number of counts in the on, off region respectively and α is the background efficiency ratio.
The TS-value for a set of model parameters ϵ can then be calculated using:

$$\text{TS} = -2 \ln \left(\mathcal{L}(\epsilon) \right) \tag{4}$$

To determine whether the model describes the data sufficiently, the significance Z is used. The significance is the probability rejecting a given null hypotheses. In this case, the hypotheses is that the respective prediction of the γ-ray emission in a region does not change the emission observed in the field of view. To determine the statistical significance the p-value is calculated. This value denotes the probability of a random generation of the observed result. If p is below a predefined value, the hypotheses can be rejected. The p-value can also be translated in the more commonly used significance Z. A general boundary for the significance is Z$= 5$, above this value a result is considered significant.
In case of nested models, the significance with which one model is preferred to the other, can be calculated as the square root of the ΔTS-value. If the parameter space of one Model can be seen as a subset of the other Model and the sample size is sufficiently large, ΔTS is χ^2 distributed with k degrees of freedom and can be used to compare two models. Here k is the difference in the number of free parameters between the two models. The ΔTS can be calculated using:

$$\Delta\text{TS} = \text{TS}_{\text{Model1}} - \text{TS}_{\text{Model2}} = -2 \ln \left(\frac{\mathcal{L}_1}{\mathcal{L}_2} \right) \tag{5}$$

If the models can not be described as nested, this work relied on adding parameters, in form of other source models, until no significant emission could be detected in the field of view.

Gammapy supports the usage of many different built-in spatial and spectral models.
The spatial models are used to estimate the morphology of the emission observed in a predefined field of view. This includes the coordinates of the center of the emission, as well as the extension of the emission. The PointSpatialModel has no extension, as it is described by an delta function centered in the pixel at the coordinates derived by the fit. If it can not be assigned to one pixel, the flux is evenly distributed across the four neighbouring pixels at these coordinates. For more extended sources, the DiskSpatialModel or the GaussianSpatialModel can be used. By default, the DiskSpatialModel describes a symmetric disk:

$$\Phi(\text{lon, lat}) = \frac{1}{2\pi(1 - \cos(\text{r}_0)} \cdot \begin{cases} 1, & \text{for } \Theta \leq \text{r}_0 \\ 0, & \text{for } \Theta > \text{r}_0 \end{cases} \tag{6}$$

with Θ the angular distance, Φ the energy flux and r_0 the radius of the disk. If an eccentricity e and a rotation angle ϕ are given, the model is called an elongated disk with a major axis r_0. The radius of the disk is chosen such that all radiation from the source is contained within. In case of a GaussianSpatialModel, the radius sigma denotes the $1\,\sigma$ containment radius. For small angular resolution and extension, the Model can be described by the formula:

$$\Phi(\text{lon, lat}) = \frac{1}{2\pi\sigma^2} \exp \left(-\frac{\Theta^2}{2\sigma^2} \right) \tag{7}$$

Similar to the DiskModel, one can also pass an eccentricity e and a rotation angle ϕ. In this case, the radius of the gaussian changes to the effective radius $\sigma_{\text{eff}} = \sqrt{(\sigma_M \sin(\Delta\Phi))^2 + (\sigma_m \sin(\Delta\Phi))^2}$ with σ_M/σ_m the major/minor axis of the Gaussian.
In this work, three different spectral Models are used, which return a flux Φ in dependence to the energy. To determine the best fit Morphology, a PowerLawSpectralModel was used in all cases. This model parametrises a power law spectrum:

$$\Phi(\mathrm{E}) = \Phi_0 \cdot \left(-\frac{\mathrm{E}}{\mathrm{E}_0}\right)^{-\Gamma} \tag{8}$$

with Γ the photon index, Φ_0 the amplitude and E_0 the reference energy. Another spectral model that is used in this work is the ExpCutoffPowerLawSpectralModel. It parametrises the energy flux, using a cutoff exponent α as well as the cutoff energy $\mathrm{E}_{\text{cut}} = 1/\lambda$:

$$\Phi(\mathrm{E}) = \Phi_0 \cdot \left(-\frac{\mathrm{E}}{\mathrm{E}_0}\right)^{-\Gamma} \cdot \exp(-(\lambda \mathrm{E})^{\alpha}) \tag{9}$$

The last spectral model used in this analysis is the LogParabolaSpectralModel. This model parametrises the flux based on a natural logarithm:

$$\Phi(\mathrm{E}) = \Phi_0 \cdot \left(-\frac{\mathrm{E}}{\mathrm{E}_0}\right)^{-\alpha-\beta\log\left(\frac{\mathrm{E}}{\mathrm{E}_0}\right)} \tag{10}$$

where β describes the curvature of the model.

In Gammapy, the spectral energy distribution is calculated using the FluxPointsEstimator. To estimate the flux in every energy bin, the amplitude of the spectral model is fitted in every energy bin independently. Using the parameter "norm", specifying the deviation between calculated flux and flux defined by the reference model, the amplitude is then re-normalized. The significance of these Fluxpoints are then calculated using the difference between the TS value of the model and the TS value without any model. If the model does not have enough excess counts in an energy bin, a upper limit is placed.

The significance maps are computed using the definition from Ti-Pei Li and Yu-Qian Ma [39]:

$$\mathrm{S}_{\mathrm{LM}} = \sqrt{2}\left(\mathrm{N}_{\text{on}} \cdot \ln\left(\frac{(1+\alpha)\mathrm{N}_{\text{on}}}{\alpha(\mathrm{N}_{\text{on}} + \mathrm{N}_{\text{off}})}\right) + \mathrm{N}_{\text{off}} \cdot \ln\left(\frac{(1+\alpha)\mathrm{N}_{\text{off}}}{\alpha(\mathrm{N}_{\text{on}} + \mathrm{N}_{\text{off}})}\right)\right)^{0.5} \tag{11}$$

To calculate the significance, the number of counts in an region containing the source N_{on} is used. This number consists of the source counts as well as the background counts in this region. To determine these background counts N_{off} a region that contains no source is chosen to estimate the number of counts. The expected ratio of the counts numbers for no source in the on-region is given by α. For $\mathrm{S}_{\mathrm{LM}} < 5$, the discovery of a source is not significant, or, in case of a prior assignment of a model to this region, the model describes the source so well that no significant emission remains after the fit.

6.2 Fermipy

The Fermi-LAT data used in this work was first assessed with the python package fermipy [40]. This package focuses on providing lucid access to the commands of the Fermi Science Tools used to evaluate LAT data. It is built on the pyLikelihood interface. This package enables to perform either an unbinned analysis, or a binned analysis. Latter is used in this work.
The SED in fermipy are computed by fitting a power-law spectra to the data for each energy bin respectively. The index of this power-law can be fixed or varied between the different energy bins. With this method, differenetial flux, energy flux and also the log-lokelihood value of the model and the 1-sigma error on the normalization are calculated.
The significance maps in fermipy are computed using the residmap() command. The significacne is calculated using:

$$\sigma_{ij}^2 = 2\mathrm{sgn}(n_{ij} - m_{ij}) \cdot \ln\left(\frac{\ln(n_{ij}) - 1}{\ln(m_{ij}) - \frac{m_{ij}}{n_{ij}}}\right) \tag{12}$$

with $m_{ij} = \sum_k (\mathrm{m}_k * \mathrm{f}_k)_{ij}$ and $n_{ij} = \sum_k (\mathrm{n}_k * \mathrm{f}_k)_{ij}$ and n_k (m_k) the data (model) maps at energy plane k and f_k the convolution kernel. This definition allows a distinction into positive and negative residuals. [41]

6.3 Data Selection

6.3.1 HESS

In this analysis only data taken during the HESS 1 era is used. Data aquired during the phase HESS 1U and HESS II were excluded, as there is only a small amount of runs available.
The quality of the data taken by the HESS telescopes is influenced by many different criteria, for example the amount of moonlight or the atmospheric conditions during the measurement. For spectral reconstruction these atmospheric conditions play an important role. The effective area and lookup tables are simulated for typical atmospheric conditions in the Khomas Highland. If the conditions deviate largely from these assumptions, a precise energy reconstruction is not possible. These runs can still be used for source detection, as no spectrum needs to be extracted. For spectral analysis, they need to be excluded. In this analysis, the runs selector of haptools, a suite of python tools useful for HESS data analysis with the collaboration internal analysis chain of HAP, was used for data selection. The minimal run duration used for this analysis is 10 minutes, to allow for sufficient statistics for the determination of proper pedestal values of the camera pixels. Only runs in which more than or equal to three telescopes measured a coincident signal were selected. The maximal Wobble offset of the telescopes from the position of HESS J1813-178 was chosen to be 2.0 degree. Allowing observations with higher offset would reduce the quality of the observations included, as the Point-spread Function of the instrument is highly correlated with the distance from the center of the Field of view and unknown for such a high offset. Therefore less livetime is more acceptable than a high offset.

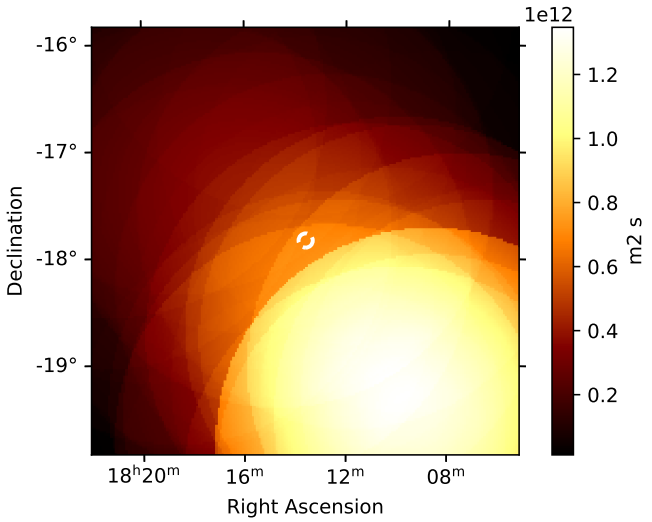

Figure 6.1: Exposure map of the data used in the analysis. The map is centered at the suspected position of the emission in the region surrounding HESS J1813-178, indicated by the white-dashed lines.

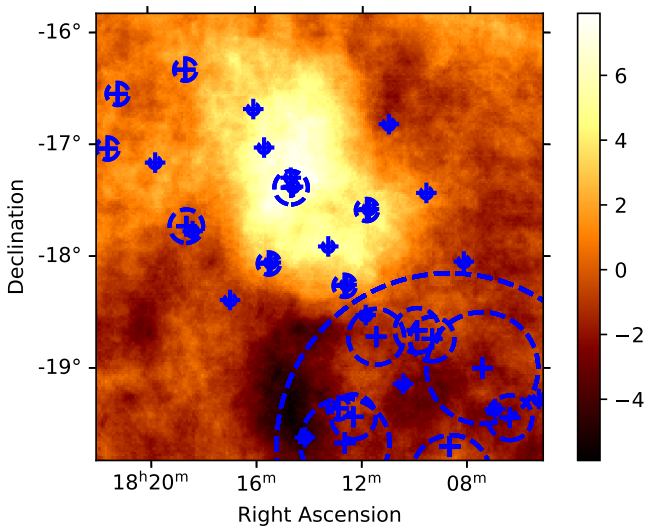

Figure 6.2: Significance map of the region after the addition of a two component model for the TeV source HESS J1809-193 and a compact component model for the TeV source HESS J1813-178. The pointing of the observation runs are indicated by the blue crosses. The amount of data taken at one pointing position is indicated by radius.

These detection criteria are chosen after an internal note by Joachim Hahn et al. and result in a runlist containing 68 runs and a total of 32 hrs of observation time.
An exposure map of the selected runs can be seen in figure 6.1.Figure 6.2 shows, a Li&Ma-significance map of the region. Here the pointing positions of the runs are indicated by a blue cross, while the radius of the circle scales with the amount of data taken at the respective positions. The map is centered at the catalogue position of HESS J1813-178. In the south-east another TeV source, HESS J1809-193 is observed. Most of the runs selected for this analysis have a high pointing-offset as they are positioned in the vincinity of HESS J1809-193. Both the distribution of the offset and the Zenith angle of the runs used for analysis can be seen in figure 6.3.
The event reconstruction was done using the ImPACT algorithm (Image Pixel-wise fit for Atmospheric Cherenkov Telescopes). This algorithm performs a maximum likelihood fit to find

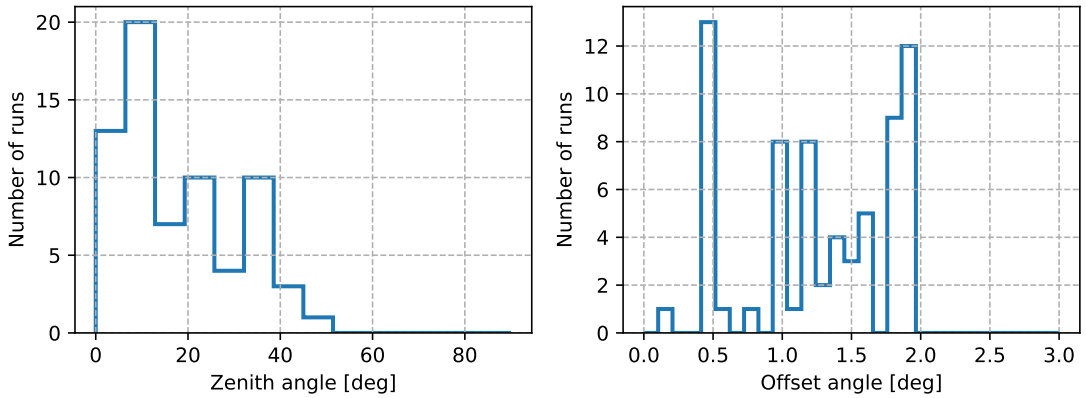

Figure 6.3: The distribution of the offset and livetime of the runs used in the analysis.

the best-fit shower parameters and results in a significant improvement of sensitivity compared to other reconstruction methods. [43] The energy binning was choosen as eight bins per decade and the pixel size of the depicted maps as 0.02°.
Before the dataset is created, a low energy threshold is applied to each run. The value of this threshold is chosen by two criteria. The first is the maximum of the energy dispersion bias threshold, which is set to the energy at which the average of the reconstructed energy is 10% above their true energy. The second criteria is the maximum of the background model rate threshold. Due to the energy threshold of the telescope, this results in a maximum in the background rate spectrum, after which the model becomes invalid. Using these two criteria, the quality of the data used for analysis can be further improved.
After this step, the background model needs to be fitted to each dataset respectively. In order to apply this background model, the dimension of the map needs to be defined first. In this analysis a square map with a side length of four degree, centered at $(273.40^\circ, -17.840^\circ)$ and a binsize of 0.02° per axis was chosen. The energy axis is logarithmically binned with 8 bins per decade between 0.3 TeV to 100 TeV. The true energy axis of the exposure is binned with 16 bins per decade in the same energy range. The background is fitted using the spectral tilt and

norm as free parameters. To ensure that only off-regions are used to estimate the background, the regions containing known sources are excluded in this step.
In the end the datasets are stacked. In this step, the point spread function and energy dispersion of each individual dataset is averaged, while counts, background and exposure are summed. In this analysis two different ways of stacking the data are compared. In the first dataset, the individual runs are projected onto the map geometry, afterwards the background is fitted to the data. Because of a high number of source regions inside the map, this method results in many runs with a low number of counts (figure 6.4a). To avoid that behaviour, the background

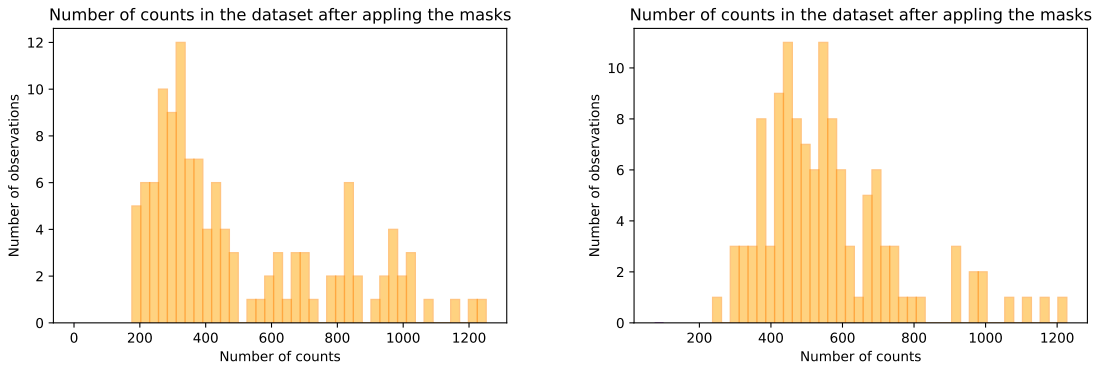

(a) (b)

Figure 6.4: The number of counts present in the respective datasets after exclusion of the on-regions containing sources depends on the pointing of the observation. Low statistics can increase the deviation of the parameters of the background fit. The Histogramm on the left shows the number of counts for the datasets after they are projected onto the map geometry. The histogram on the right shows the same number before the projection.

is fitted to the respective runs before they are stacked onto the map geometry. This results in a higher number of counts per dataset (figure 6.4b). To exclude the possibility of broken pixel or other statistical processes, the distribution of the norm and tilt parameter of the background model are checked after the fit. They are expected to show a normal distribution around zero for the tilt and around one for the spectral norm. The achieved mean value of the distribution can be seen in figure 6.5. Both the mean and the deviation of the parameters are acceptable and the dataset can then be used for the analysis.

parameter of the bkg fit for fitting the whole data in the observation

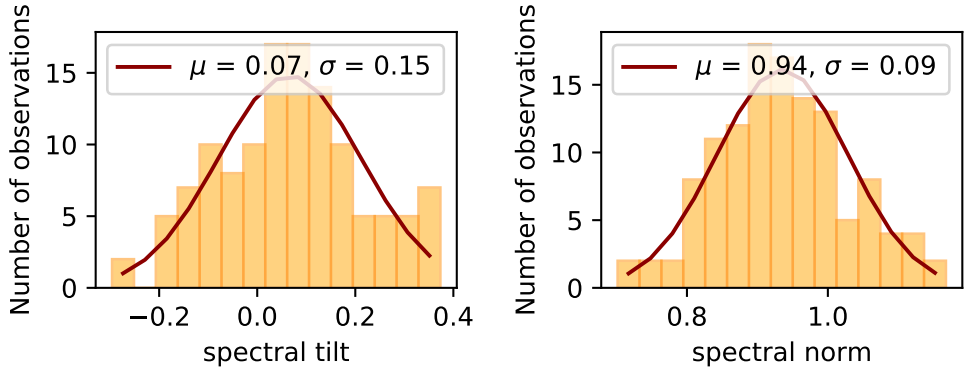

Figure 6.5: The distribution of the background parameters is expected to be a gaussian distribution centered around one for the spectral norm and around zero for the spectral tilt.

6.3.2 Fermi-LAT

For the Fermipy analysis 13 years of off-pulse observation data is used. The field of view for the LAT dataset is chosen as 6 degree, with a binsize of 0.025°. The energy axis chosen for this dataset ranges from 1 GeV to 1 TeV with 8 energy bins per decade. The IRFs used in this analysis are PASS 8, with the corresponding background models, iso_P8R3_SOURCE_V2_v1.txt, which describes the isotropic diffuse emission and the gll_iem_v07.fits model, describing the emission originating in the galactic center.
This data is first analyzed using Fermipy. Afterwards the data is extrapolated and further analyzed in gammapy. The dataset used for the gammapy analysis has a slightly larger field of view (10°x10°) because the evaluation of the sources outside of the FOV is different between the two analysis packages. While Fermipy includes sources with emission extending into the FOV, gammapy would usually not take this emission into account. After creation of the instrument response functions, the data is masked to 6x6 degree for the analysis and the energy range is extended by one more bin below 1 GeV and above 1 TeV. Additionally the models from the sources within the field of view are fitted using the 4FGL source catalogue.

7 Morphological and Spectral Studies

The goal of this study is to identify the nature of the emission that can be observed in the region around the TeV source HESS J1813-178. A first indication of this nature is gained by the morphology and spectral shape, with which the observed emission can be described. This analysis also allows for an investigation of the discrepancy in extension between the Fermi-LAT and HESS data.

7.1 The region around HESS J1813-178

The γ-ray emission coming from the region around HESS J1813-178 was identified as a single source, that is describable using a gaussian source model, with an extension of sigma $= 0.04^\circ$ and a spectral index of $\Gamma = 2.09 \pm 0.08$ during the galactic plane survey of HESS. This survey also reports an extended emission in this region that is discarded because of a detection threshold below $5\,\sigma$ and their goal being to find new point-like sources. [13]

First, after the creation of the dataset described above, the number of excess counts, as well as the Li&Ma- Significance for each pixel in the field of view is calculated. The results for each pixel is then stacked onto the analysis geometry. The Li&Ma significance in each pixel of a

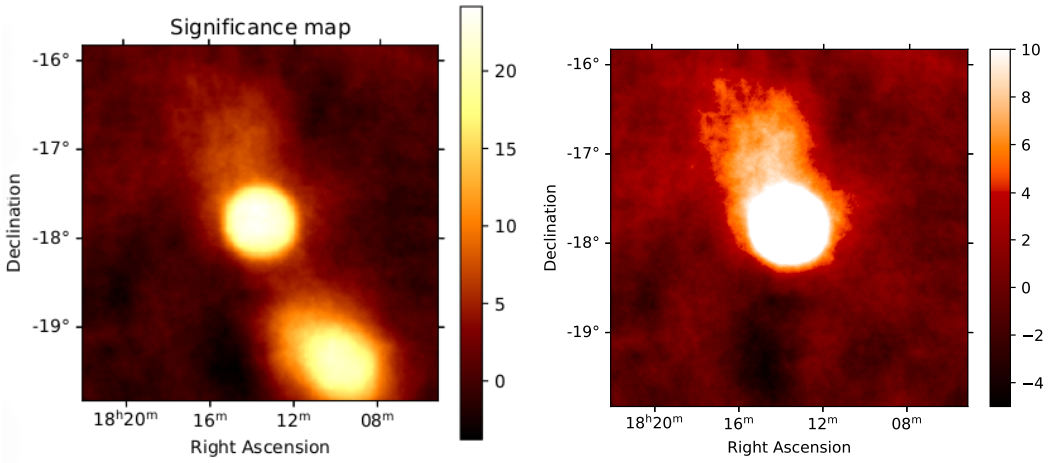

Figure 7.1: The significance is calculated using the Li&Ma-method [39]. On the left: Significance map of the region centered on the catalogue position of HESS J1813-178. On the right: The emission in the field of view after the best-fit model from an internal HESS-analysis of the emission attributed to the TeV source HESS J1809-193 is taken into account.

4°x4° region around the catalogue position of HESS J1813-178 can be seen in the left plot in figure 7.1.
The emission that can be observed in the center of the map is coincident with the position of PSR J1813-1749, which was suggested as the origin of the electrons producing the high energy

γ-rays in previous analysis. The TeV source HESS J1809-193 is located in the south-west, along the galactic plane, at a small projected distance from HESS J1813-178. The emission from this TeV source can also be seen in the left plot in figure 7.1. The best-fit source model for the emission attributed to HESS J1809-193 has been derived in an internal analysis done by Lars Mohrmann. After the addition of this source model, the significance was calculated again and visualized in the right plot in figure 7.1. The best-fit values of both components are indicated by the white-dashed lines.

To identify the best description of the emission in the region around HESS J1813-178, different spatial and spectral models were applied in systematically increasing complexity. After the addition of the respective source models, the amount of residual emission for every model was compared. In the beginning, the spectral model was fixed to a Power Law, to avoid an unnecessary addition of degrees of freedom. After the addition of the model, the significance for each pixel is computed. The significance is then visualized. Additionally, the significance

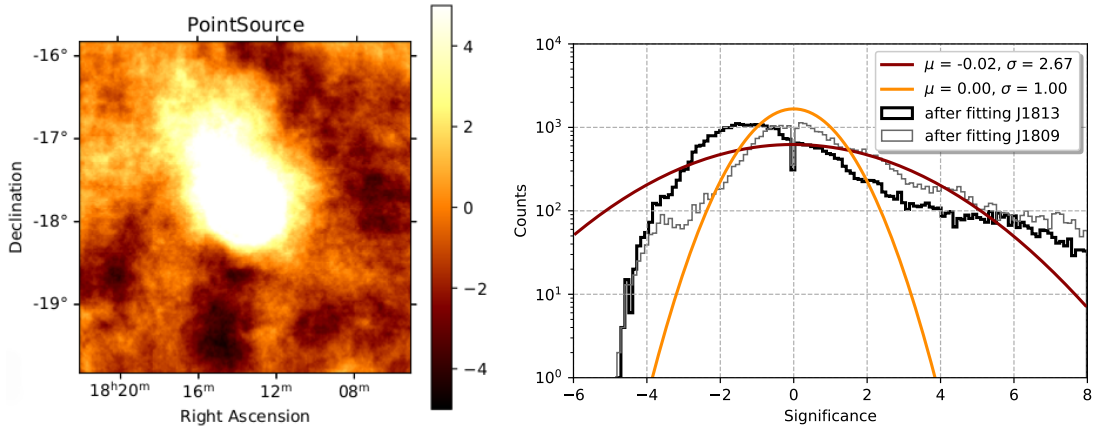

Figure 7.2: Significance map and significance distribution of the region after the point source model is fitted to the data. The grey line in the plot on the right indicates the significance distribution before the addition of the model for HESS J1813-178. The orange gaussian curve indicates a distribution with no remaining emission left in the field of view, the red gaussian curve is the fit-curve to the observed distribution.

distribution is visualized in a histogram. For each case, the distribution before the addition of the source model and after the addition is compared. Additionally, the python package scipy is used to perform a least-square minimization to the distribution. In case of no remaining emission in the source region, the distribution is dominated by the random fluctuations of the significance. This results in a gaussian distribution with a mean of $\mu = 0$ and a standard deviation of $\sigma = 1$.

The respective model was added to the data and a likelihood minimization is performed. Then, the significance map of the region after the addition of the source model is calculated. The first morphological hypothesis that is tested for this region, is that the γ-ray emission can be

described by a Point source. The significance map and distribution can be seen in figure 7.2. The best-fit least square of a gaussian distribution can be seen in red in the plot on the right, the fit parameters are denoted in the legend. The distribution before the addition of the source model is indicated by the grey histogram. The point source model can not describe the emission from the source adequately, the source is extended. In order to find a better description, a disk model as well as a gaussian source model were applied to the data. The width of the significance distribution decreases from $\sigma = 2.25$ for the diskmodel, to 2.12 for a gaussian source model, therefore the gaussian source is chosen as the best description of the emission in the area. The best-fit position (table 1), agrees within a $1\,\sigma$ level with the position derived in the

Parameter	Best-fit value	Error	Unit
R.A.	273.40	0.004	deg
Dec.	-17.831	0.004	deg
Sigma	0.067	0.004	deg
Amplitude	3.767	0.185	$10^{-12}\,\mathrm{TeV}^{-1}\mathrm{cm}^{-}2\mathrm{s}^{-1}$
Index	2.187	0.042	-

Table 1: The best-fit parameters for the compact gaussian source model.

galactic plane survey [13], the extension found in this analysis is slightly more extended then observed during the survey, but the deviation is below $3\,\sigma$. At lower energies, the spectrum and SED of this analysis (figure 7.3) agree with an analysis of the region conducted in 2007 [14]. At energies above $10\,\mathrm{TeV}$ deviations can be observed. These deviations can be attributed to the low systematics of the dataset at high energies due to the small number of observations of the region, as well as changes in the background model between the two analysis. The gaussian source model describing the emission from the TeV source HESS J1813-178 found in this analysis agrees with the results derived in a previous analysis of the source.
After finding the best description for the morphology, the spectral model is varied. Besides the Power Law model, a LogParabola Model and an Exponential Cutoff model are used. Adding two more degrees of freedom in the form of an Exponential Cutoff model does not improve the model. The LogParabola is preferred over the Power Law model with a significance of $1.5\,\sigma$. Because the addition of the parameter β does not improve the description of the area significantly, the Power Law model is chosen as the spectral model for the compact source HESS J1813-178 for the further examination of the area.

The significance map computed after the addition of the compact gaussian source (left plot in figure 7.4), show residual extended emission towards the north-east, along the galactic plane. This emission region is very extended with its centered slightly askew to the compact source. The significance distribution of the residual emission after the addition of the compact gaussian source can be seen in the right plot in figure 7.4. With an standard deviation of $\sigma = 2.12$, the distribution shows that the residual emission is significant.

The detection of this extended source allows the possibility of a continuous description of the

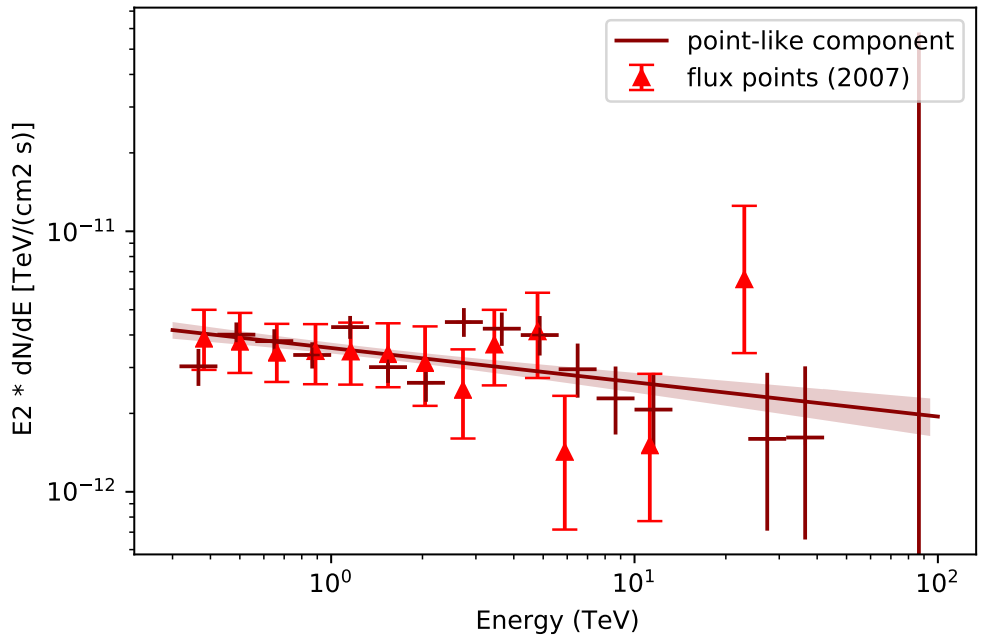

Figure 7.3: The SED derived in this work compared to the SED derived in the analysis of this region done in 2007 [14] can be seen on the left.

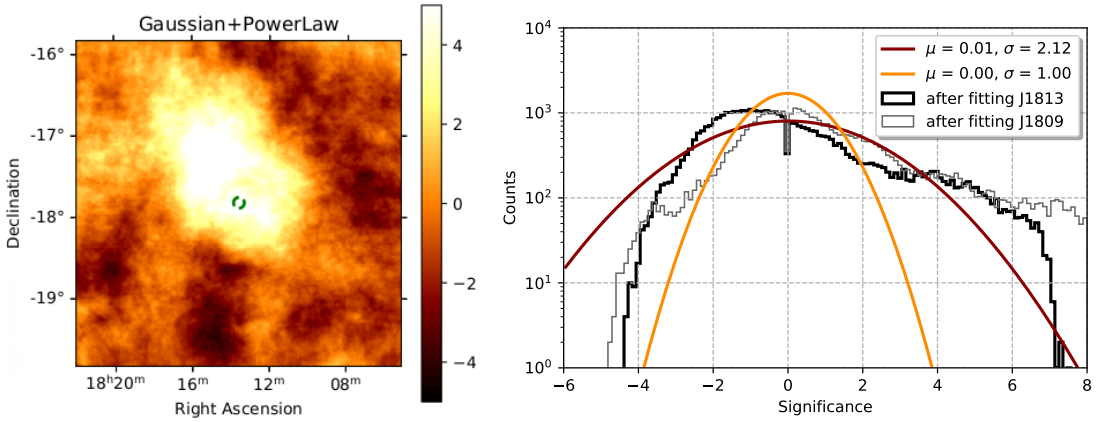

Figure 7.4: The best description of the emission can be achieved using a gaussian source. The residual emission in the region after the addition of the gaussian source model can be seen in the significance map on the right. The extension and position of this model are indicated by the green circle. The significance distribution can be seen on the left.

region between instruments, over a broad energy range. In order to achieve this, the best-fit model for the HESS data needs to be derived first. This is done analogous to the derivation of

the model of the compact component. At first, the spectral model is fixed to a Power Law, four different spatial models are tested. The residual significance maps after the addition of these source models are shown in figure 7.5. The model added to derive the respective significance

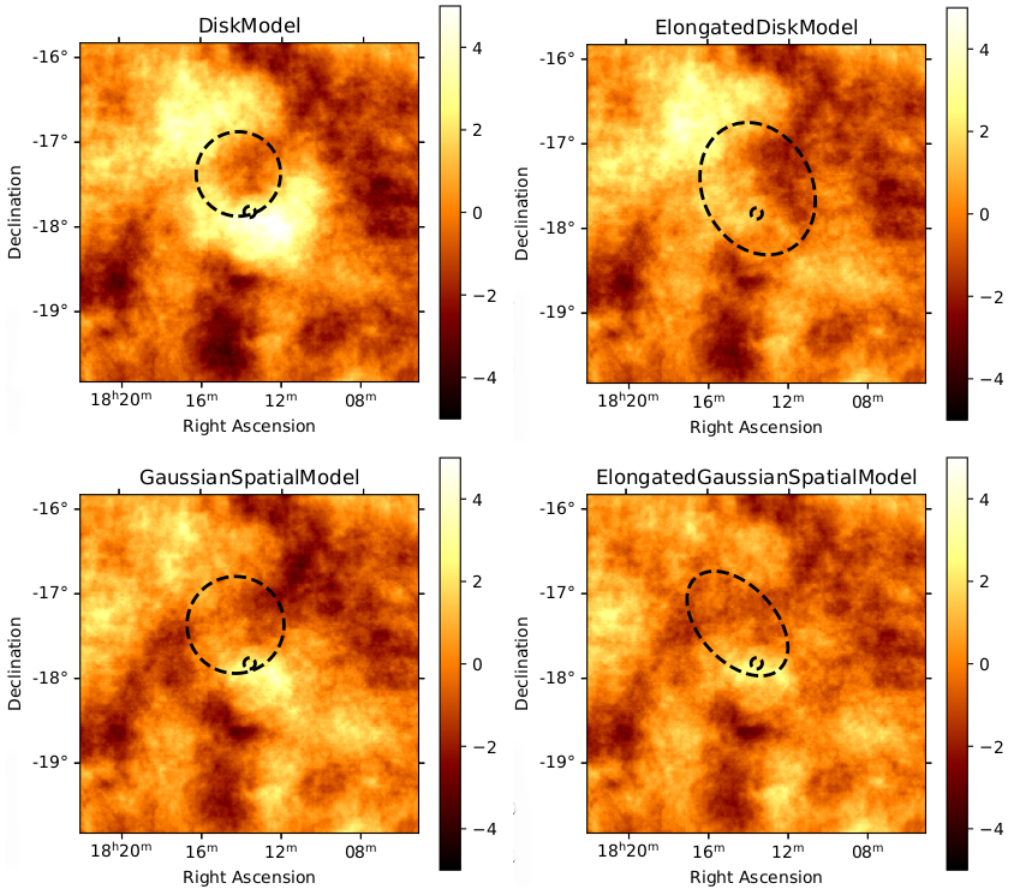

Figure 7.5: To describe the remaining emission in the field of view after the addition of the compact gaussian model, four different spatial models are used to estimate the best description. The model used can be seen in the caption of the respective map, the best-fit parameters are indicated by the black-dashed lines.

is described in the headline of the map.
This extended diskmodel has a singificance of 13.18σ. The addition of this model is not a good description, as it leaves a significant amount of emission in the north-east and south-east from the compact component. Because of this elliptical shape of the remaining emission, the symmetric diskmodel is exchanged for an elongated diskmodel. This elongated model is preferred over the symmetric model with a significance of $7.83\,\sigma$, but can not describe the excess to the north-east. Because neighter models can fully describe the observed extended emission, a gaussian source model is applied to the data. The width of the significance distribution in the case of a diskmodel is $\sigma = 1.59$. After the addition of the gaussian source, the width decreases

to $\sigma = 1.21$. The gaussian can describe the emission better than the diskmodel. To account for the remaining emission after the gaussian source is applied, two additional parameters are added to the model. Even though the improvement from the symmetric gaussian source to the

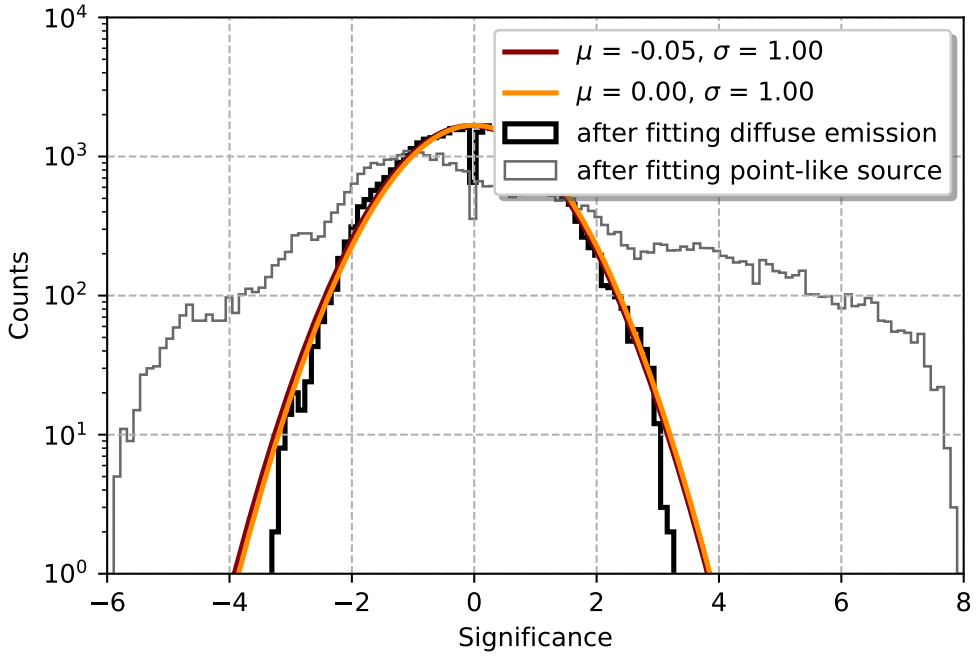

Figure 7.6: The significance distribution after the addition of a compact gaussian source model and an elongated gaussian source model. There is no emission above $5\,\sigma$ left.

elongated gaussian is only $3.34\,\sigma$, the improvement of the significance distribution 7.6, which is flat after the addition of the elongated source warrants the addition of the two degrees of freedom. The best-fit parameters of this source model can be seen in table 2. The compact gaussian source HESS J1813-178 and the extended elongated source are a good description of the emission in the region of HESS J1813-178. The elongated gaussian is chosen as the spatial model in the further analysis.

After the identification of the best-fit morphology, the spectral model is varied. The Power Law spectral model is exchanged for a LogParabola model and an Exponential Cutoff model. Similar to the compact component, the Exponential Cutoff model is not a good description, the Power Law yields better results. The addition of the LogParabola also does not yield better results, the improvement of the description is $0.006\,\sigma$. The Power Law is chosen as the preferred model to describe the extended emission. The spectra of both components can be seen in figure 7.7. The spectral energy distribution of the compact component shows a steeper decline at high energies, above an energy of 8 TeV no significant fluxpoint can be computed. For the extended component, a significant fluxpoint is derived at 86.6 TeV, the spectrum seems to extend to tens of TeV without a spectral break or cutoff.

Parameter	Best-fit value	Error	Unit
R.A.	273.630	0.064	deg
Dec.	-17.374	0.069	deg
Semi-Major Axis	0.727	0.080	deg
Eccentricity	0.802	0.061	deg
Position Angle	221.110	7.370	deg
Amplitude	9.939	1.384	$10^{-12}\,\mathrm{TeV}^{-1}\mathrm{cm}^{-}2\mathrm{s}^{-1}$
Index	2.288	0.075	-

Table 2: The parameter values of the best-fit source model for the observed extended emission.

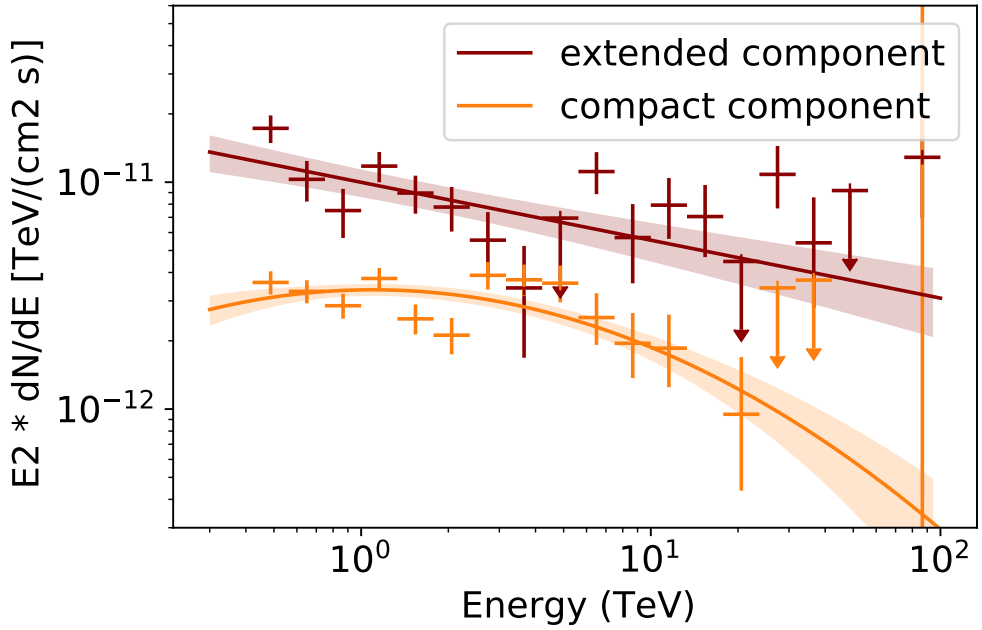

Figure 7.7: The energy flux of the compact and extended component.

To explore the energy dependence of the two component model, the data is divided into four energy bins (0.4 to 1 TeV, 1 to 3 TeV, 3 to 10 TeV, 10 to 100 TeV). The above derived models are then added to each dataset respectively and the significance map and distribution are examined (figure 7.8).

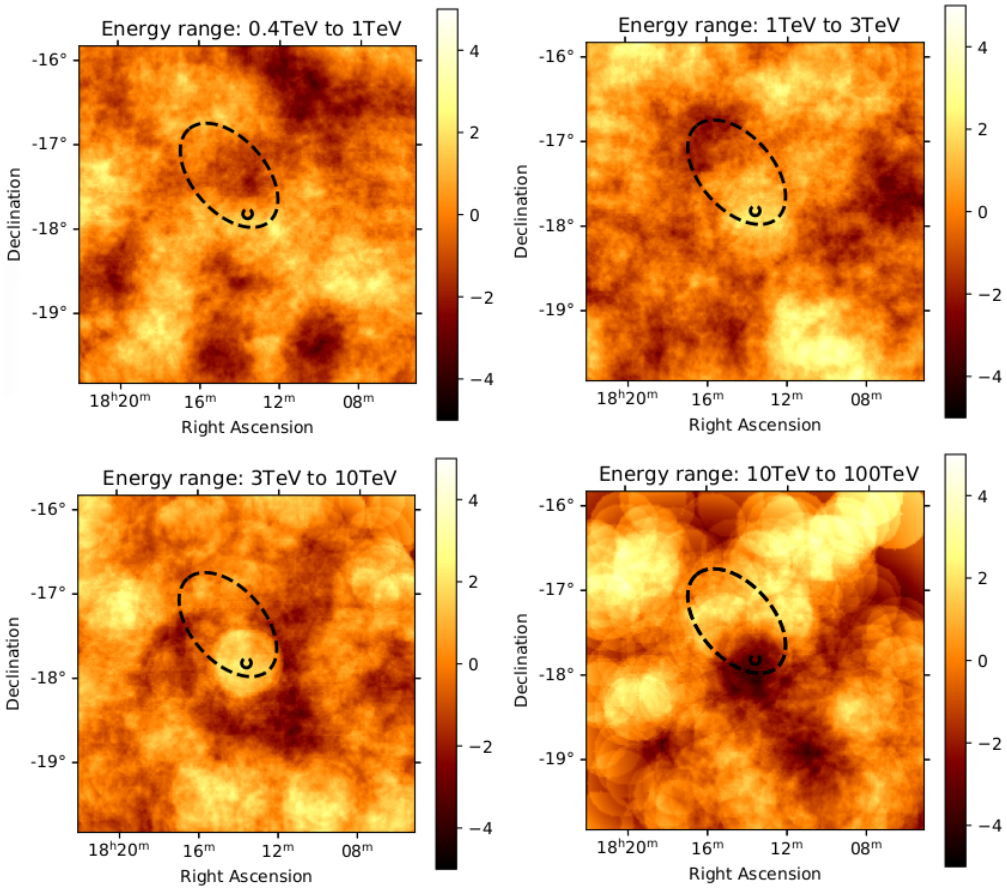

Figure 7.8: In order to estimate the goodness of the fit for different γ-ray energies, the best-fit parameters are frozen and the model is applied to the data in different energy bins.

In the energy range between $0.4\,\text{TeV}$ to $10\,\text{TeV}$, the two component model with the derived parameters describe the emission well, the residual maps are flat. In the energy range from $10\,\text{TeV}$ to $100\,\text{TeV}$, residual emission can be observed above a latitude of -17.5°. This residual emission is attributed to the low statistics at high energies because of the small amount of observation runs that can be used for this analysis. Therefore it is concluded that the description of the emission in the region around HESS J1813-178 with a compact and an extended source is sufficient in all energy ranges.

The last analysis of the region containing HESS J1813-178 with Fermi-LAT was done in 2018 [18]. With the detection of the extended emission in HESS, the description of the region is both instruments similar. To estimate if the best-fit morphology derived in the old analysis of the LAT data can be used to describe the emission observed by HESS, it is applied to the HESS data. The morphology of the model is fixed and the spectrum fitted. The compact component it fixed to the best-fit values derived in this analysis. A significance map and distribution is calculated. The spectrum connects smoothly to the SED derived in the LAT analysis, but with

a mean of $\mu = 0.25$ and $\sigma = 2.00$, the significance distribution is not flat. This description can not account for the strong emission to the north-east from the position of the pulsar. The spectrum resulting from the description using the elongated gaussian is also compared to the SED derived in 2018. The Energy flux of the extended component is higher than the flux derived in 2018.
To achieve a continuous description of the region from GeV to TeV energies, the Fermi-LAT data of this area is reanalyzed.

7.2 The region around 4FGL J1813.1-1737e

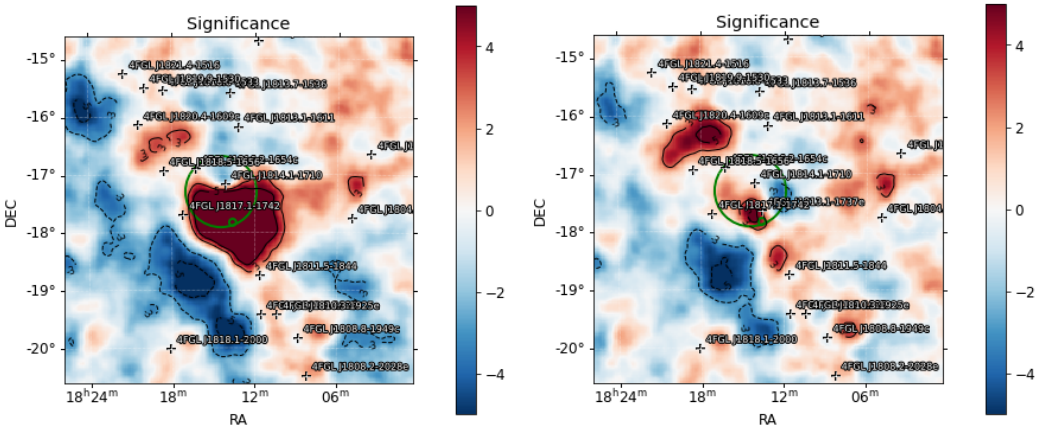

Figure 7.9: An significance map of the region surrounding the source HESS J1813.1-1737e in a 6°x6° field of view. The map on the left side shows the region without a model for HESS J1813.1-1737e, while the 4FGL catalogue model is included for the creation of the right significance map.

The current catalogue model used for the source 4FGL J1813.1-1737e, associated with the TeV source HESS J1813-178 is a one component, RadialDisk model at a position of RA $= 273.29^\circ$ and Dec $= -17.62^\circ$ with an extension of 0.6°.
For the analysis, the python package fermipy, which facilitates the analysis of the data from Fermi-LAT with the Fermi Science Tools, is used. After the creation of the counts cube and IRF cubes, the known sources in the field of view are modeled using the respective description from the 4FGL source catalogue. Additionally, the galactic and isotropic background model are applied to the data. After the application of all models, the region is optimized by iteratively fitting the normalization and spectral shape parameters of all models in the region of interest (ROI). Then the TS value of all sources is calculated and weak sources with a TS < 4 are removed from the model.

After the optimization of the region, the position of the source, as well as the spectral parameters of all sources within a distance of 5° of 4FGL J1813.1-1737 are refitted. Significance maps of the region with and without this source model can be seen in figure 7.9. The RadialD-

isk with an LogParabola spectral model does not describe all emission that can be attributed to 4FGL J1813.1-1737e. Due to the restriction that the Science Tools can only do a spatial or spectral likelihood-minimization separately as well as the support of only symmetrical models, the open source tool gammapy is preferred as an analysis tool also for the Fermi-LAT data.
To use gammapy as a tool to evaluate data taken by the Fermi-LAT, the differences between this tool and the Science tools need to be considered. After increasing the ROI and adding two

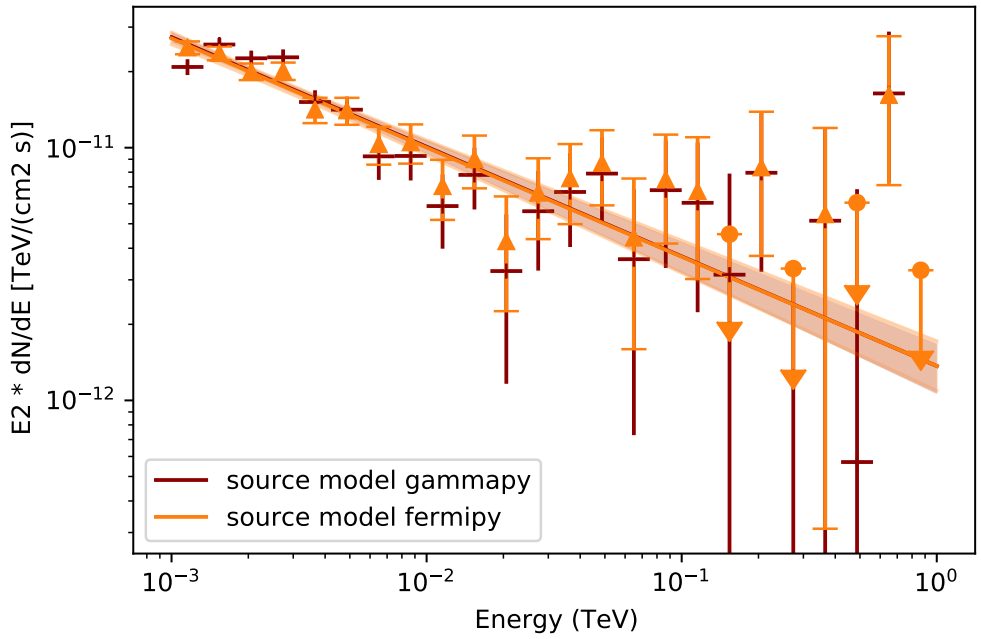

Figure 7.10: The spectral parameters of the source 4FGL J1813.1-1737e derived in gammapy are equal to the parameters derived in fermipy within the error.

energy bins, as described above, the counts cube and IRF cube for this geometry are created. The spatial and spectral models of the background sources are translated to fit the standard models used in gammapy. The diffuse isotropic background can be used in gammapy without any adjustments. After taking the exposure in every pixel into account, the galactic diffuse background map provided by the Fermi Collaboration is mapped onto the counts map geometry. The emission is described by a Power Law model with normalized amplitude. Then a safe mask is applied to the data, to reduce the ROI to the same extension used in the analysis done with fermipy. Also the additional energy bins are masked. To ensure that all source models are correctly interpreted in gammapy, the source model for 4FGL J1813.1-1737e was not extrapolated from the analysis done by fermipy. The gammapy model corresponding to the Fermi-LAT catalogue model is added to the data and a likelihood-minimization is performed. The result can be seen in figure 7.10. To ensure comparability to the analysis done with the Science tools, the spatial parameters are frozen to the best-fit values derived in fermipy. The best-fit values of the spectral parameters are equal within $1\,\sigma$. Additionally, the number of predicted counts is derived for both background models and the source model (left plot in figure 7.11). The num-

ber of predicted counts matches for the galactic diffuse background, as well as for the source model for 4FGL J1813.1-1737e. The deviation of the predicted counts for the isotropic diffuse background is within a $1\,\sigma$ error. The same comparison was done for all background sources in the field of view. An respective example for this comparison can be seen in the right plot in figure 7.11 for the source 4FGL J1817.1-1742. The number of predicted counts matches for all sources in the field of view.
After confirming the correctness of this extrapolation, gammapy can be used for further analysis. In the beginning, the spectral model is changed form a Logparabola to a Power Law. Then best-fit spatial model is derived analogous to the analysis of HESS J1813-178. Because of a simultanious fit of morphology and spectrum, an improvment can already be seen by fitting all source parameters with the Diskmodel. The standard deviation of the singificance distribution decreases and in the histogram of the significance distirbution no entry in a bin above $5\,\sigma$ is left. The best results are again achieved by adding an elongated gaussian source for 4FGL J1813.1-1737e. It is preferred over the symmetric gaussian with a significance of $3.6\,\sigma$. The significance map and distribution after the addition of this model can be seen in figure 7.12. An indication of a second, compact component that is positionally coincident with the component observed in HESS is found, but no detection can be claimed, due to a significance of the compact component below 5σ.
The data is then again evaluated with a LogParabola as a spectral model using the elongated morphology. The substitution of the spectral model brings an improvement of $2.61\,\sigma$. The description of the emission using an exponential cutoff model is $0.13\,\sigma$ more significant. The spectral energy distribution of the extended component (figure 7.13) is, at energies below $10\,\mathrm{GeV}$ softer than observed in the previous analysis of the 4FGL source [18], but follows the same shape as the spectrum derived in an analysis done by Xin & Guo [20]. The shape of the SED indicates that a simple, predefined spectral model is not enough to describe the source in this energy range.

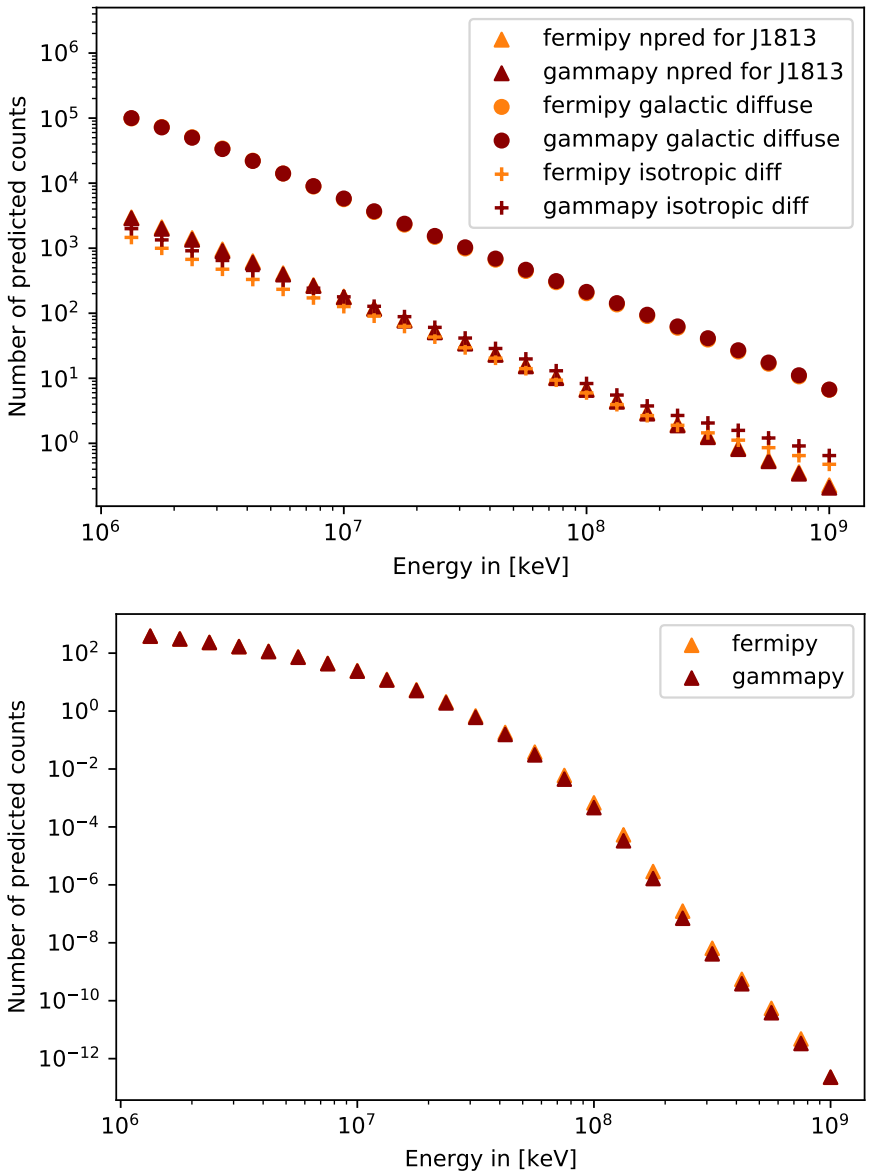

Figure 7.11: In the top: the predicted counts for the background models, as well as the predicted counts of the source model for 4FGL J1813.1-1737e, derived in fermipy and gammapy. In the bottom plot: The predicted counts derived by both analyisis tools for the bacckground source 4FGL J1817.1-1742.

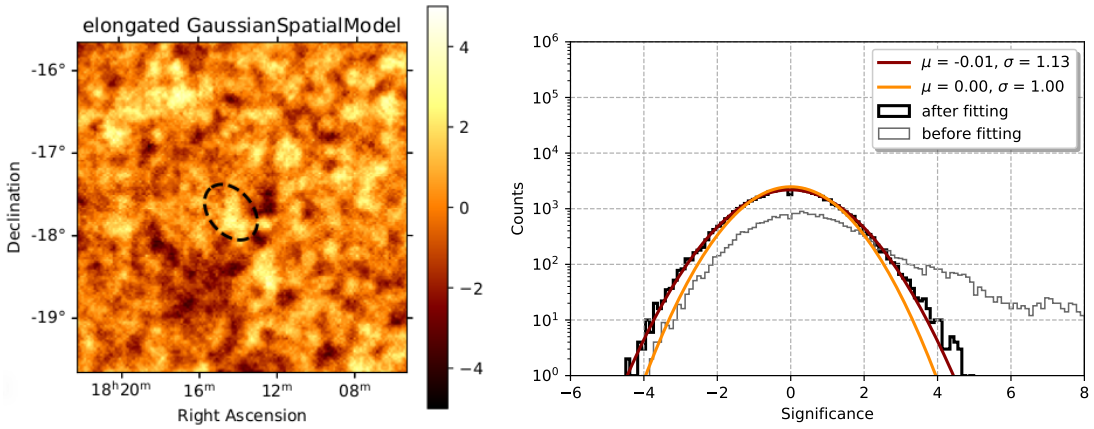

Figure 7.12: The signficance map and distribution after the additon of an extended elongated gaussian source model with a Power Law as spectral model. The emission in the region around 4FGL J1813.1-1737e can be described by one component in the GeV energy range.

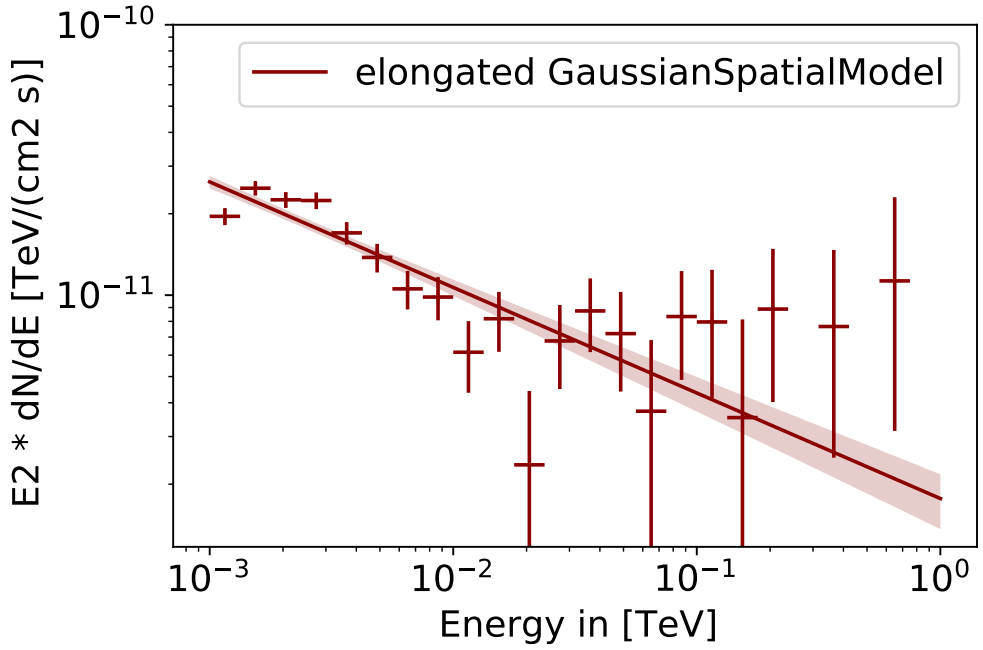

Figure 7.13: The spectrum and SED of the elongated gaussian source model. The shape of the SED suggests a soft spectral index below 20 GeV and a hard index above this energy. The Power Law model can not describe this behavior.

7.3 Joint-Fit

After analyzing the the observation data in the respective energy ranges separately, a joint-analysis covering five decades in energy, is performed. For this purpose the respective datasets are combined. Using this method, it is possible to apply the same source model to the data acquired by different telescopes and perform a binned maximum likelihood fit of the combined observation data. In case the resulting source model can not describe the emission sufficiently, instrument related effects might play a role and need to be investigated.
After the combination of the datasets from HESS and Fermi-LAT, the source models of the background sources are added to the dataset. Then the symmetric gaussian and the elongated gaussian source model for the region surrounding HESS J1813-178 are applied to the dataset. The high surface brightness of the gaussian source model describing the emission from the compact component, makes an addition of this model to the combined data necessary, even though no detection can be claimed in the energy range below $0.4\,\mathrm{TeV}$. An explanation for not detecting the compact source in the Fermi-LAT data is a spectral break to lower energies or a steep spectral slope. A LogParabola model with curvature of $\beta = 0.11$, as derived in the HESS analysis, would be sufficient to explain this behaviour.
Because of the shape of the spectral energy distribution derived in the separate analysis of the source, a LogParabola model is chosen as the spectral model of the extended emission. The dif-

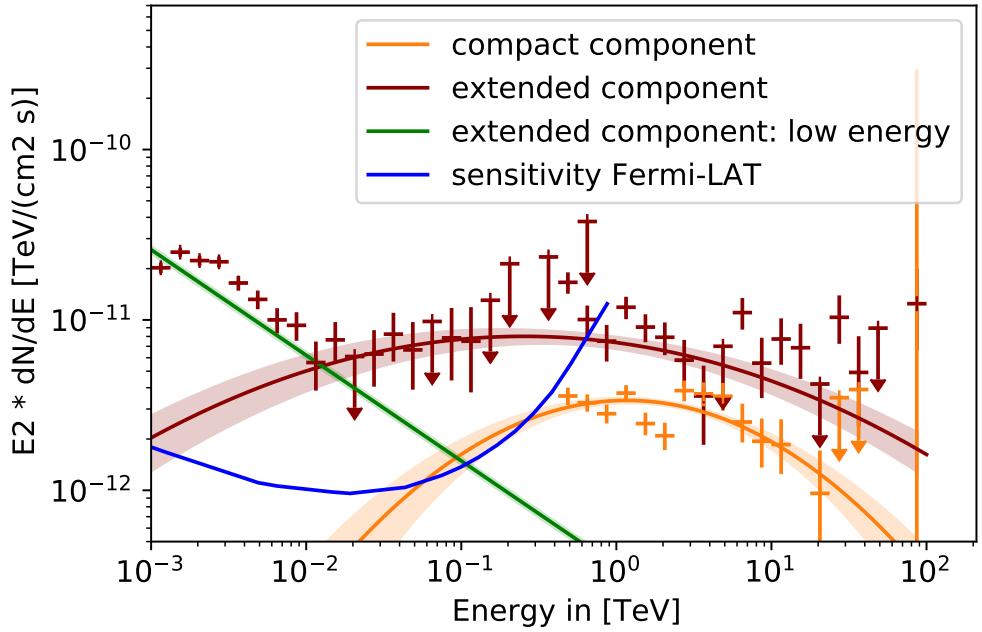

Figure 7.14: The shape of the SED spectrum can be described by a Power Law describing the extended component in the lower energies and two LogParabola models describing the extended elongated source and the compact gaussian source at higher energies. The blue curve indicates the sensitivity threshold of the PASS 8 instrument response function of Fermi-LAT [61]

ferent morphology and spectral index at lower energies poses a problem in this analysis. After the addition of the two components, the significance maps are not flat. The derived spectrum does not follow the behaviour of the spectral energy distribution. Because of this observation and the presumption of a different origin of the emission below 10 GeV, a third source model, an elongated gaussian model with a Power Law spectral model, is added to the combined data. The addition of this third source model results in a good description of the region. The computed significance maps are flat and the spectral parameters are in agreement with the spectral energy distribution. The best-fit values of the source model parameters can be seen in table 3. The source model describing the emission at low energies is extended with $\sigma = 0.36^{\circ}$, while the emission at higher energies has an extension of 0.71°.
Additionally to the spectra and Fluxpoints, the broadband sensitivity curve of Fermi-LAT for the Pass 8 instrument response functions [61] is visualized as a blue curve in figure 7.14. If the assumption of a logparabolic shape of the emission of the compact component is correct, the energy flux is lower than the sensitivity of Fermi below roughly 70 GeV. Above 70 GeV, the statistics of the measurement are limited and the energy flux is marginally higher than the senisitivity limit of Fermi. This observation is in good agreement with the non-detection of the compact component. The component describing the soft, low energy emission is less extended than the component describing the emission at higher energies. The soft spectral index below 20 GeV, as well as the slightly different morphology, indicate the γ-rays in this energy range might have a different production mechanism. The residual maps in the respective energy ranges are flat after the addition of the sources. The spectrum matches the shape of the SED derived in the respective analysis (figure 7.14).

The γ-ray emission from the region around the TeV source HESS J1813-178 can, in the TeV energy range, be described by an compact gaussian source and an extended elongated gaussian source. The best-fit model for the source 4FGL J1813.1-1737e, associated to HESS J1813-178, is also an elongated gaussian source, with a smaller extension than the source observed in HESS. With these results, no continuous description of the region over five decades of energy can be claimed. Including the joint-analysis, it becomes apparent that the extended emission can be described by two seperate sources, an smaller elongated gaussian source at lower energies and an more extended elongated source at high energies. The description of the region with three source models allows an good description of the spectral energy distribution from the region, as well as a consistent description of the morphology between the two instruments.

Parameter	Best-fit value	Error	Unit
R.A.	273.460	0.012	deg
Dec.	-17.708	0.012	deg
Semi-Major Axis	0.355	0.015	deg
Eccentricity	0.805	0.025	deg
Position Angle	226.360	2.355	deg
Amplitude	0.357	0.024	$10^{-12}\,\mathrm{TeV}^{-1}\mathrm{cm}^{-}2\mathrm{s}^{-1}$
Index	2.620	0.000	-
R.A.	273.400	0.047	deg
Dec.	-17.382	0.043	deg
Semi-Major Axis	0.603	0.053	deg
Eccentricity	0.705	0.076	deg
Position Angle	210.700	6.957	deg
Amplitude	7.365	0.724	$10^{-12}\,\mathrm{TeV}^{-1}\mathrm{cm}^{-}2\mathrm{s}^{-1}$
Alpha	2.122	0.055	-
Beta	0.045	0.000	-
R.A.	273.400	0.002	deg
Dec.	-17.832	0.002	deg
Sigma	0.057	0.003	deg
Amplitude	3.360	0.180	$10^{-12}\,\mathrm{TeV}^{-1}\mathrm{cm}^{-}2\mathrm{s}^{-1}$
Alpha	1.963	0.050	-
Beta	0.121	0.029	-

Table 3: The best-fit parameters of the joint-fit. The first set of parameters describes the extended source at lower energies, the second set are the best-fit parameters for the extended component at higher energies and the last set describes the compact source.

8 Energy Dependence of the derived Morphology

Describing the extended emission with a smaller gaussian source and a more extended gaussian component indicates an energy dependence of the morphology of the source. In the analysis of many extended TeV γ-ray sources, such an energy-dependence of the morphology was observed [46], [47], [48], [49], [50].

8.1 HESS J1813-178

To examine the energy dependence of the morphology of the region around HESS J1813-178, the two component model is applied to the data in different energy bins. The best-fit values of the parameters are then compared. In order to achieve a precise result, the energy bins chosen should only enclose small energy ranges. Because of the small amount of observation data on HESS J1813-178, a fine binning is not possible. The energy bins are chosen as 0.4 to 1 TeV, 1 to 3 TeV, 3 to 100 TeV. The significance maps computed after the addition of the two compo-

nent source model can be seen in figure 8.1, with the best-fit morphology indicated by the black dashed lines. The extension and center position the compact component is within 1σ errors

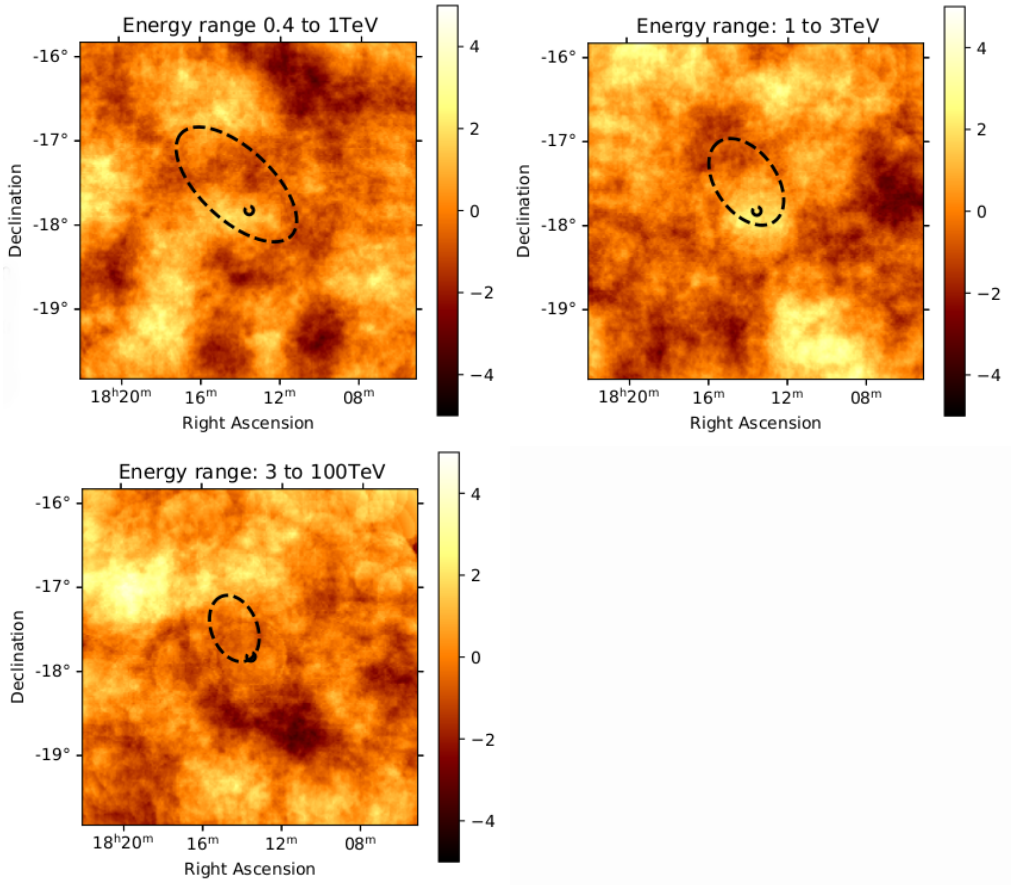

Figure 8.1: In order to test for an energy dependent morphology, the best-fit models are refitted in different energy bins. The resutling morphology is again depicted by the black-dashed lines.

equal in all energy bins, no energy-dependence can be observed. As indicated by the best-fit positions in figure 8.1, the morphology of the extended emission depends on the energy bin. In order to visualize the observed variability, the distance between the center of the elongated source and the position of PSR J1813-1749, the suspected origin of the emission, is calculated. The best-fit value of the semi-major axis is then plotted over this distance (figure 8.2). The error on the position is calculated using gaussian error propagation with the error values estimated in the log-likelihood minimization.

The distance of the center of the extended γ-ray emission to PSR J1813-1749 does not depend on the energy. Despite the coarse energy binning, an indication of an decreasing extension of the source with increasing photon energy can be observed.

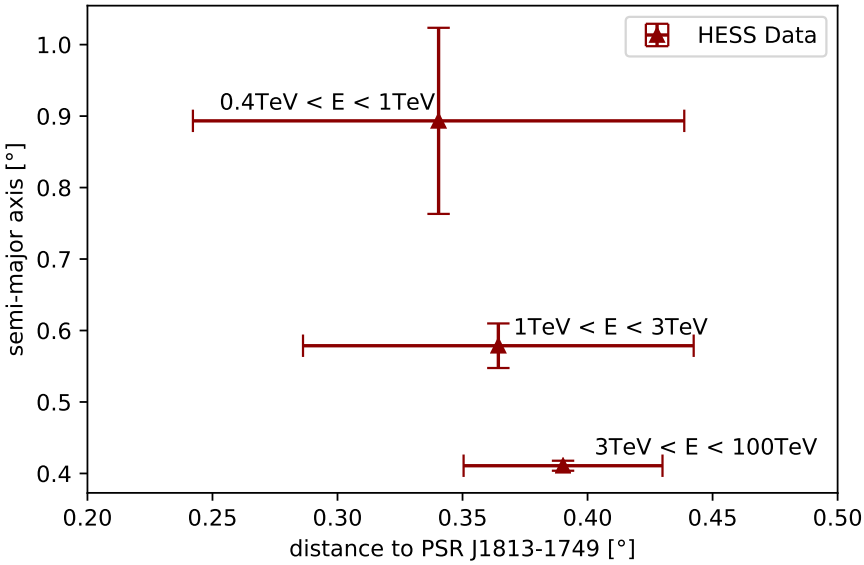

Figure 8.2: The area of the best-fit morphology in the respective energy bin is plotted over the distance of the center of the ellipse to the pulsar located within the structure.

8.2 4FGL J1813.1-1737e

In the TeV energy range, HESS J1813-178 shows an indication of an energy dependent morphology, even though the statistics of the observations are low. Applying a similar analysis for the data from the Fermi-LAT, allows an observation of the extension of the emission over a larger energy range.
The data was again divided into energy bins and the best-fit model applied to the data. The spectral energy distribution of 4FGL J1813.1-1737e implies a soft spectral index below 10 GeV and a hard spectral index above 10 GeV. This behaviour indicates that the emission below the spectral break might have a different origin than the emission observed above 10 GeV. Therefore the data was divided into three energy bins below 10 GeV and three bins above the spectral break (table 4). The model was applied to the respective data and the best-fit extension derived. This extension is then compared to the distance of the centroid from PSR J1813-1749. The results can be seen in figure 8.3. Additionally to the extension of the emission in the GeV energy range, the results of the analysis in the TeV emission is depicted. The resulting datapoints are labeled with a number corresponding with the energy range in which they are computed. The datapoint labeled with 1 corresponds to the first energy band etc., while, for the HESS data, the first energy band is labeled as H1 and the rest analogous. This analysis shows that no energy dependence can be observed for the emission below 10 GeV. The center of the emission also does not shift position in this energy range within the 1σ error. The errors on the parameters derived above 10 GeV are large because of the low statistics of Fermi-LAT at high energies. Nevertheless, a trend can be observed. The best-fit value of the semi-major axis of the elongated gaussian model is increasing with increasing energy. With this development, a

Energy bin	minimum Energy [GeV]	Maximum Energy [GeV]
1	1.00	1.78
2	1.78	3.16
3	3.16	7.50
4	7.50	17.78
5	17.78	56.23
6	56.23	$1.00 \cdot 10^3$
H1	$0.42 \cdot 10^3$	$1.00 \cdot 10^3$
H2	$1.00 \cdot 10^3$	$3.16 \cdot 10^3$
H3	$3.16 \cdot 10^3$	$100 \cdot 10^3$

Table 4: The energy bins used to calculate the energy dependence of the morphology of the extended emission in the region surrounding HESS J1813-178

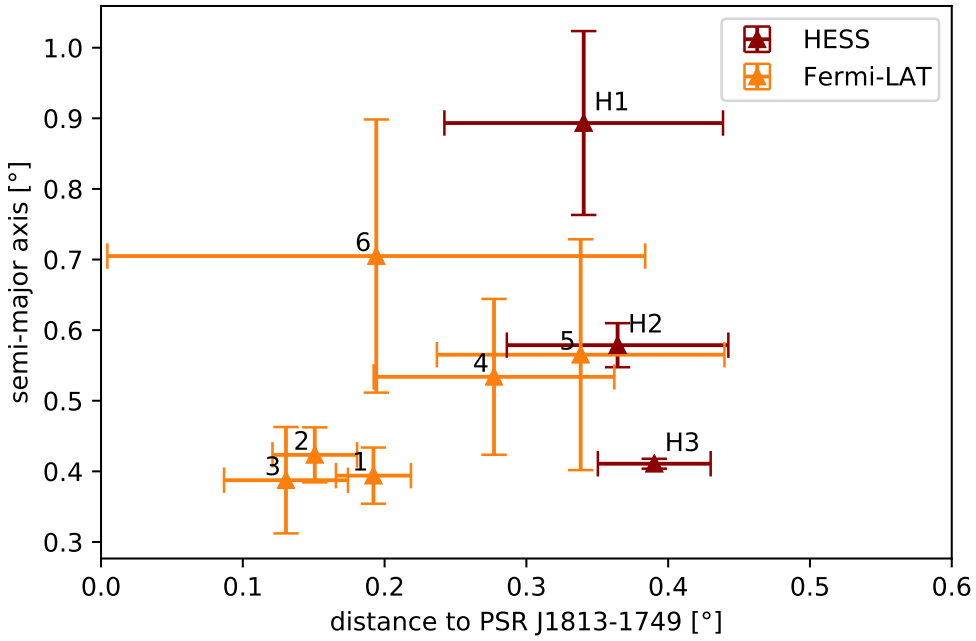

Figure 8.3: The best-fit value of the semi-major axis plotted over the distance to the pulsar. The data from Fermi-LAT indicates that the size of the emission increases with energy and in the TeV range decreases with energy.

consistent morphological description of the region surrounding HESS J1813-178 between the Fermi-LAT data and the HESS data is achieved.

9 Multi-Wavelength studies of the region

In previous studies of the source an influence of the star-froming region W33 on the evolution of the pulsar wind nebula surrounding PRS J1813-1749 has been suggested. With the estimation of a distance of 6 to 12 kpc of the pulsar, this claim can no longer be considered. Nevertheless, the multiwavelenght context of the region is important to understand the physical processes in the region. To better visualize the position of W33, as well as the supernova remnant G012.8-00.0, in respect to the extended emission, the contours of the radio emission are plotted in the counts map of the HESS data. The radio observations used in this analysis were obtained by the Very Large Array. The focus of these observations was the supernova remnant G012.8-00.0, therefore the data does not contain the whole emission from W33. The radio contours (red) in respect to the best-fit morphology of the TeV emission (white) can be seen in the left plot in figure 9.1. The emission from W33 extends further to the south-west then depicted. The

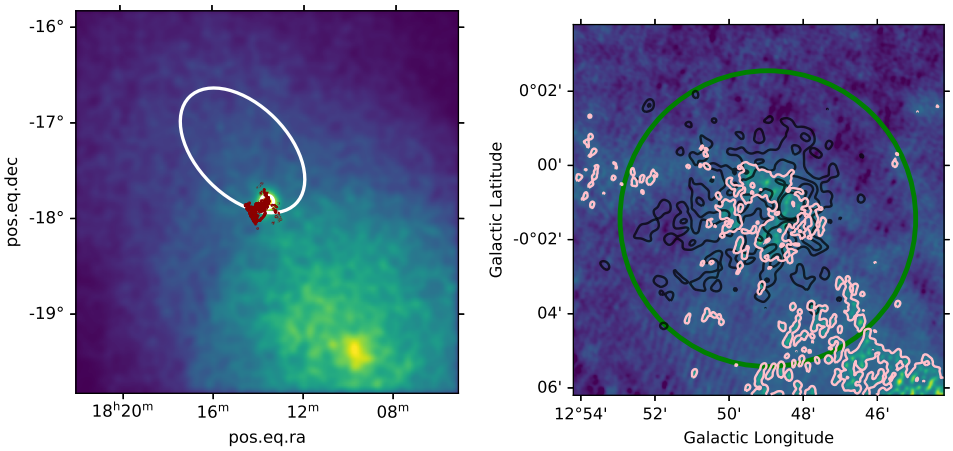

Figure 9.1: On the left: Counts map of the TeV data, with contours of the radio data obtained by VLA in red. The best-fit morphology is indicated in white. On the right: The radio data obtained by the VLA, overlayed by the contours of the compact TeV source HESS J1813-178 derived in this analysis. The TeV contours are displayed in green, the contours of the VLA data are displayed in pink, and the x-ray data taken by the ASCA satellite are plotted in black.

compact component is positionally coincident with the shell-like structure of the supernova remnant. To better visualize this, the plot on the left in figure 9.1 shows a cutout of the VLA data (pink), overlayed with the contours of the best-fit morphology of the compact source component HESS J1813-178 in green. Additionally, the x-ray data taken with the ASCA satellite is displayed in black. Both the x-ray emission attributed to PSR J1813-1749 and the radio emission from G012.8-00.0 is located within the extend of the compact component HESS J1813-178. The pulsar has not yet left the the supernova remnant, indicating a young age, or a small tangential velocity.

10 Particle diffusion in the region

In order to get a better understanding of the nature of the observed extended emission, the radial profile of the cosmic-ray energy density in the region is investigated. The radial distribution of cosmic rays $\omega_{\mathrm{CR}}(\mathrm{E}, \mathrm{r}, \mathrm{t})$ can be observed as constant, if the particles are injected by a single burst-like event. In case of a continuous injection of particles by an accelerator and a stable diffusion coefficient in the region, the radial distribution follows a $\omega_{\mathrm{CR}}(\mathrm{E}, \mathrm{r}, \mathrm{t}) \propto 1/\mathrm{r}$ dependence, while $\omega_{\mathrm{CR}}(\mathrm{E}, \mathrm{r}, \mathrm{t}) \propto 1/\mathrm{r}^2$ can be observed for advection in a wind. [51] To determine the behaviour of the cosmic rays in the region surrounding HESS J1813-178, the flux in six circular regions with a radius of 0.2° along the axis of the extended emission is estimated. Then, using the formula $\sum_i \mathrm{data}_i/(\pi \mathrm{r}^2)$, the flux per area is calculated and plotted over the distance to PSR J1813-1749 (figure 10.1). This profile indicates that a continuous injection of

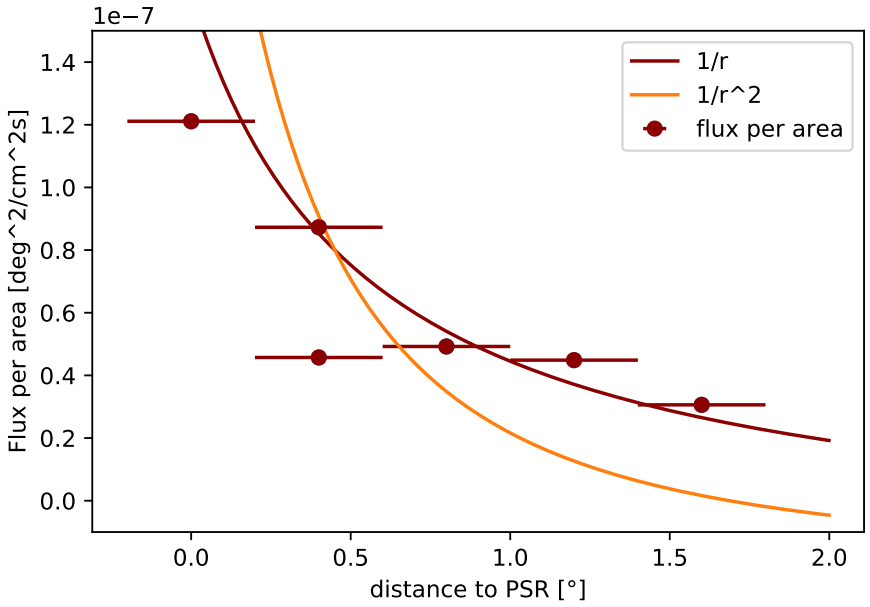

Figure 10.1: Spatial distribution of cosmic ray flux plotted over the distance to PSR J1813-1749. The horizontal errorbars show the bin size. A fit to the data following a $1/\mathrm{r}$ distribution is depicted by the red line, while a fit following a $1/\mathrm{r}^2$ distribution is shown in orange.

particles is preferred over the $1/\mathrm{r}^2$ behaviour.

11 Discussion

In previous analysis of the region, a leptonic origin of the compact γ-ray emission from HESS J1813-178 was favoured, though a hadronic origin could never be excluded. With the discovery of the extended component the region becomes more complicated and the previously derived results have to be reevaluated. More detailed analysis and spectral modelling are needed to explain the origin of the observed high energy γ-ray emission. However, some important conclusions can already be drawn from this analysis.

The spectral analysis of the TeV emission yields a soft spectrum of the compact component HESS J1813-178 at high energies. In case of a leptonic origin of the γ-ray emission, this spectral softening at the high energies is expected, due to Klein-Nishina (KN) suppression of the electrons. At lower electron energies, in the Thomson regime ($\eta = \mathrm{E_{ph}E_e}/(\mathrm{m_e}c^2)^2 \ll 1$) , electron cooling occurs and, given enough time, an equilibrium between injection and energy loss can be observed. This equilibrium results in a roughly continuous energy flux. In the Klein-Nishina regime ($\eta \gg 1$), relativistic effects result in a smaller interaction cross section and the scattering is no longer elastic with a small momentum transfer, but is deeply inelastic and shows a large momentum transfer. The electrons lose most of their energy in a single collision, resulting in a soft energy spectrum at high energies. Therefore, observing this rapid softening of the spectral energy distribution is a good indication that the origin of the compact TeV emission has a leptonic origin. [44] This is in agreement of previous analysis of the source, the emission most likely represents the pulsar wind nebula of PSR J1813-1749. [14], [16]
The spectral analysis of the extended TeV component yields a significant fluxpoint at 86.6 TeV. Because of the limited statistics, the errorbar on this fluxpoint is large, and no definitive conclusions about the steepness of the spectral index of the emission can be made from the energy flux detected at this energy. Should more observation data prove that the energy flux measured in this range is correct and decrease the errorbar, a hard spectral index is implied. This hard spectral index at high energies is a good indication for a hadronic origin of the emission. Because of the relation $\mathrm{P_{IC}} \propto 1/\mathrm{m}^4$ with $\mathrm{P_{IC}}$ the energy loss of the particle and its mass m, a higher energy loss is expected for lighter particles. The Klein-Nishina suppression sets in later for a proton spectrum.
However, Breuhaus et al. [45] recently proposed the possibility of hard spectral indices in TeV energy spectra of leptonic origin. Breuhaus et al. [45] argues that these spectral features can be observed at regions containing a powerful pulsar ($\dot{\mathrm{E}} > 10^{36}$ erg/s) and a homogeneous soft photon field. Additionally, such a spectrum requires strong magnetic fields or particle diffusion away from the pulsar with small energy loss. Breuhaus et. al. [45] concludes that the necessary parameters for such a ultra high energy IC-emission can not be met in typical environments. As possible candidates they propose the galactic disk, inside of spiral arms or in regions of intense far-infrared emission e.g. present in regions of active star formation. This leptonic scenario with γ-ray emission up to 100 TeV has not been verified yet, but recently obtained results from the LHAASO observatory support the possibility of such spectra [44].

In former analysis of the region, an association between the stellar cluster Cl 1813-178 in the

star-forming region W33 and the pulsar PSR J1813-1749, and therefore also an association with the TeV emission, was made. This stellar cluster could provide the far-infrared emission necessary for the observed hard emission, but because of recent distance estimates favouring a distance between 6 and 12 kpc to the pulsar and a distance of 4.8 kpc to the stellar cluster [52], W33 can not be seen as the birthplace of the pulsar and the stellar cluster has no influence on the emission resulting from PSR J1813-1749.
Two scenarios of the origin of the extended emission are possible. The positional coincidence between PSR J1813-1749, the supernova remanant G12.82-0.02 and the γ-ray emission favours a leptonic scenario with the pulsar as injection source. Both, in the GeV and in the TeV energy range, the emission of the extended component is extended towards the north-east from the position of the pulsar. The displacement of the center of the extended emission and the position of the pulsar indicate irregularities in the ambient medium. The inhomogeneous density of the surrounding medium causes an uneven extension of the supernova shock. Therefore, the reverse shock that forms displays an irregular shape and meets the pulsar wind nebula at different times. This results in a distortion of the observed emission. In case of a distance of the pulsar of ≈ 4 kpc, the stellar cluster Cl 1813-178 could be considered as the necessary irregularity in the ambient medium, but with the new distance estimation no interaction is possible. The second scenario is that there is no association between the extended high energy γ-ray emission and the pulsar. The TeV emission is located in the vicinity of the stellar cluster. The stellar cluster, a formation of massive stars inside a giant molecular cloud, presents many acceleration sites for cosmic rays, such as collective stellar winds and supernova explosions inside the cluster, possibly accelerating cosmic rays up to PeV energies. These cosmic rays can then scatter of molecular hydrogen clouds, producing localised and intense γ-ray emission. [62] Using the spatial and spectral analysis of the γ-ray emission, neither of the scenarios can be excluded.
The radial profile of the cosmic-ray energy density in the region of the extended TeV emission supports both scenarios. It suggests an continuous injection of particles into the region. In an leptonic scenario this continuous injection is powered by the electrons and positrons accreted from the pulsar surface and accelerated in the wind termination shock. In a hadronic scenario the combined emission from the stellar cluster represents a continuous provider of cosmic rays, with an continuous acceleration in the stellar cluster wind-driven shocks.

An indication favouring the leptonic origin of the high energy γ-ray emission in the region around HESS J1813-178 is the observation of an energy-dependent morphology. The decrease of extension of the observed emission with energy can be observed in many pulsar wind nebulae. [46], [47], [48], [49], [50]., but not for an hadronic emission originating in the supernova remnant. After the relativistic wind of particles is accelerated in the proximity of the pulsar, different processes can be responsible for an energy loss, leading to the decrease in size with an increase in energy. The young, high energy particles are released into the system from the open magnetic field lines of the pulsar. They can be found in the vicinity of the pulsar. As they age, these particles propagate away from the pulsar through diffusion or advection. The extension of the observed γ-ray emission increases. During propagation, the particles loose energy through radiative cooling of the electrons, including adiabatic expansion, ionisation losses,

bremsstrahlung, synchrotron losses and inverse Compton scattering. Therefore, older particles with less energy can be observed at higher distances from the pulsar. Additional process resulting in an energy dependence of the extension of the emission are an energy dependent injection spectrum as well as an energy dependent diffusion or convection speed.
The energy dependence observed in the TeV energy range agrees with this theory, and a hint of a decrease of extension with increasing energy is observed in this analysis. Because of the small amount of observation data available, resulting in low statistics, the size of the energy bins used to estimate the extension needs to be chosen coarsly and the errorbars on the resulting best-fit parameters are large. This observed energy-dependence is not conclusive to exclude a hadronic origin of the TeV emission, but indicates that a leptonic scenario is favoured.
In the GeV energy range, the morphology behaves differently. The soft, low energy emission below 10 GeV is located in the vincinity of the pulsar and shows no energy dependence, which would, in a leptonic scenario, imply that the effect of diffusion of the electrons responsible for this emission is neglectable, they lose energy without propagating away from the pulsar. In the energy range above 10 GeV a trend of an increase in angular extension can be observed, but due to the large error bars no definitive statement can be made. Presumed the observed trend is correct, the increase in size of the emission above 10 GeV can be explained by pure diffusion. The electrons are emitted by the pulsar and propagate without losing energy, up to a certain distance. Then the ambient medium changes and electron cooling starts, resulting in the decrease of extension observed in the TeV energy range. Such a peak in extension at a roughly 1 TeV has also been observed in the system of the Geminga pulsar. [60] This trend would imply that the low energy electrons show only small diffusion but high cooling rate, while the higher energy electrons diffuse without cooling. This indicates that the observed emission can not be described by a simple leptonic process, and justifies the addition of a third source model to describe the region over five decades of energy.

The observations made in the analysis of the high energy γ-ray emission in the region around the TeV source HESS J1813-178 suggest an association of the high energy emission with the pulsar PSR J1813-178. The spectral break at high energies of the compact TeV component, as well as the observed positional coincidence of the pulsar and the TeV emission, are in agreement with previous analysis suggesting an leptonic origin of the emission. The extended component shows to different behaviours. The emission at low energies shows a soft spectral shape and no energy depenenet morphology, while the emission at high energies shows a hard spectral shape, an energy depenent morphology and a coninuous injection spectrum. This indicates two different γ-ray production mechanisms in the extended emission. A leptonic origin of the emission is favoured, but a hadronic scenario can not be excluded.

12 Summary and Outlook

In this work, the data of the region surrounding the TeV source HESS J1813-178 and the associated GeV source 4FGL J1813.1-1737e was reanalyzed. A second extended emission component is detected in the TeV energy range. This extended component is positionally coincident with the pulsar PSR J1813-1749, which is believed to be the source of the TeV emission and also with a stellar cluster Cl J1813-178.
This work shows that with this newly detected extended emission component a continuous description of the region above five decades of energy, from $1\,\mathrm{GeV}$ to $100\,\mathrm{TeV}$, is possible. For this continuous description three source models are necessary. A compact gaussian source with an Logparabola spectral model to account for the emission from HESS J1813-178, as well as two source models to account for the emission from the extended source. A elongated gaussian source with an Powerlaw for the soft emission below $10\,\mathrm{GeV}$, and an elongated gaussian source with an Logparabola spectral model describing the emission above $10\,\mathrm{GeV}$.
Additionally, the behaviour of the extended emission component was analyzed. The cosmic-ray density profile of the region shows that the TeV emission is powered by a continuous injection. The extension of the best-fit model of the extended emission was observed in different energy ranges. This observation shows that the size of the emission first increases with increasing energy, until roughly $0.4\,\mathrm{TeV}$. At higher energies, the extension of the emission decreases with increasing energy.
Two possible origins of the high energy γ-ray emission were proposed. A leptonic scenario with an association of the extended emission to PSR J1813-1749 and an hadronic scenario, in which the extended emission is a result from the interaction of cosmic rays accelerated in the stellar cluster with a molecular cloud located in the vicinity. The hadronic scenario could not be excluded with certainty, but the observation of an energy dependent morphology favours the leptonic scenario.
In this thesis, a total of $30\,\mathrm{h}$ of observation data was used. Because of this low amount of data and the location of the source in a complicated region directly on the galactic plane, the results derived can only be seen as preliminary. More observation data has been requested, but is still pending. Additionally, a physical model for the observed emission needs to be estimated in the future. With this model, the origin of the emission can be further constrained and the parameters of the system can be estimated.

References

[1] **V. F. Hess**, MEASUREMENTS OF THE PENETRATING RADIATION DURING SEVEN BALLOON FLIGHTS, *2018,(Translated and commented by A. De Angelis and C. Arcaro b. Schultz)* https://arxiv.org/pdf/1808.02927.pdf

[2] **M. Tanabashi et. al.**,Review of Particle Physics*, *2018, Physical Review D, Volume 98* https://ui.adsabs.harvard.edu/abs/2018PhRvD..98c0001T/abstract

[3] **G. T. Zatsepin, V. A. Kuzmin**, Upper Limit of the Spectrum of Cosmic Rays, *2009, Journal of Experimental and Theoretical Physics Letters, Volume 4* https://ui.adsabs.harvard.edu/abs/1966JETPL...4...78Z/abstract

[4] **K. Greisen**, END TO THE COSMIC-RAY SPECTRUM?, *1966, Physical Review Letters, Volume 16* https://arxiv.org/pdf/1808.02927.pdf

[5] **M. Bustamante et. al.**, High-energy cosmic-ray acceleration, *2009, presented during the 5th CERN Latin American School of High-Energy Physics.* https://cds.cern.ch/record/1249755/files/p533.pdf

[6] **S. Funk**, Ground- and Space-Based Gamma-Ray Astronomy, *2015, Annual Review of Nuclear and Particle Science, Volume 65* https://www.annualreviews.org/doi/pdf/10.1146/annurev-nucl-102014-022036

[7] **A. Heger et. al.**, How Massive Single Stars End Their Life, *2003, The Astrophysical Journal, Volume 591* https://ui.adsabs.harvard.edu/abs/2003ApJ...591..288H/abstract

[8] **Manami Sasaki**, Extreme Astrophysics, *2020, FAU Summer Semester, Chapter 10*

[9] **B.M.Gaensler, P.O.Slane**, The Evolution And Structure Of Pulsar Wind Nebulae, *2006, Harvard-Smithsonian Center for Astrophysics* https://arxiv.org/pdf/astro-ph/0601081.pdf

[10] **W. Bednarek, M. Bartosik**, Gamma-rays from the pulsar wind nebulae, *2003* https://www.aanda.org/articles/aa/pdf/2003/26/aa3605.pdf

[11] **Patrick Slane**, Pulsar Wind Nebulae, *2017* https://arxiv.org/abs/1703.09311

[12] **Oleg Kargaltsev, Benoît Cerutti, Yuri Lyubarsky, Edoardo Striani**, Pulsar-Wind Nebulae: Recent Progress in Observations and Theory *2015, Space Science Reviews 191* https://www.researchgate.net/publication/280104803Pulsar-WindNebulaeRecentProgressinObservationsandTheory

[13] **Aharonian et. al.**, The H.E.S.S. Survey of the Inner Galaxy in Very High Energy Gamma Rays, *2006, The Astrophysical Journal, Volume 636, Issue 2* https://ui.adsabs.harvard.edu/abs/2006ApJ...636..777A/abstract

[14] **Funk et. al.**, XMM-Newton observations of HESS J1813-178 reveal a composite Supernova remnant, *2007, Astronomy and Astrophysics, Volume 470, Issue 1* https://arxiv.org/abs/astro-ph/0611646

[15] **E. V. Gotthelf, J. P. Halpern**, DISCOVERY OF A HIGHLY ENERGETIC X-RAY PULSAR POWERING HESS J1813-178 IN THE YOUNG SUPERNOVA REMNANT G12.82-0.02, *2009, The Astrophysical Journal, Volume 700* https://arxiv.org/abs/0907.0137

[16] **Jun Fang, Li Zhang**, MULTIBAND NONTHERMAL RADIATIVE PROPERTIES OF HESS J1813-178, *2010, The Astrophysical Journal, Volume 718* https://iopscience.iop.org/article/10.1088/0004-637X/718/1/467/meta

[17] **F. Acero et. al.**, Constraints on the Galactic Population of TeV Pulsar Wind Nebulae Using Fermi Large Area Telescope Observations, *2013, The Astrophysical Journal, Volume 773* https://ui.adsabs.harvard.edu/abs/2013ApJ...773...77A/abstract

[18] **M. Araya**, GEV EMISSION IN THE REGION OF HESS J1809-193 AND HESS J1813-178: IS HESS J1809-193 A PROTON PEVATRON?, *2018, The Astrophysical Journal, Volume 859* https://ui.adsabs.harvard.edu/abs/2018ApJ...859...69A/abstract

[19] **J. Albert et. al.**, MAGIC Observations of Very High Energy γ-Rays from HESS J1813−178, *2006, The Astrophysical Journal, Volume 637* https://iopscience.iop.org/article/10.1086/500364/meta

[20] **Yu-Liang Xin, and Xiao-Lei Guo**, The γ-ray emission toward HESS J1813-178 with Fermi-LAT, *2021, Proceedings if Science, ICRC 2021* https://pos.sissa.it/395/625/pdf

[21] **Petr Tràvnìcek**, Detection of high-energy muons in cosmic ray showers, *2004,Doctoral theses*
https://inspirehep.net/literature/673493

[22] **H.J. Völk, K. Bernlöhr**, Imaging very high energy gamma-ray telescopes, *2009, Experimental Astronomy, Volume 25* https://link.springer.com/article/10.1007/s10686-009-9151-z

[23] **H.Abdalla et. al.**, The H.E.S.S. Galactic plane survey, *2018, Astronomy & Astrophysics, Volume 612* https://www.aanda.org/articles/aa/fullhtml/2018/04/aa32098-17/aa32098-17.html

[24] **W. Hofman**, The H.E.S.S. Telescopes, *2012* https://www.mpi-hd.mpg.de/hfm/HESS/pages/about/telescopes/

[25] **K. Bernlöhr, O. Carrol, R. Cornils, et. al.**, The optical system of the H.E.S.S. imaging atmospheric Cherenkov telescopes Part I: layout and components of the system, *Astropart. Phys., 20:111128, Nov. (2003)* https://arxiv.org/pdf/astro-ph/0308246.pdf

[26] **Kornelia Stycz**, VHE Gamma-Ray Sources at the Resolution Limit of H.E.S.S., *Dissertation, 06.2015* https://edoc.hu-berlin.de/bitstream/handle/18452/18169/stycz.pdf?sequence=1

[27] **S. Funk, G. Hermann, J. Hinton, et al.**,The trigger system of the H.E.S.S. telescope array, *Astropart. Phys., 22:285296 (2004)* https://arxiv.org/pdf/astro-ph/0408375.pdf

[28] **M. Holler , D. Berge, C. van Eldik, J.-P. Lenain, V. Marandon, T. Murach, M. deNaurois, R.D. Parsons, H. Prokoph, D. Zaborov**, Observations of the Crab Nebula with H.E.S.S. Phase II, https://arxiv.org/pdf/1509.02902.pdf

[29] **A. A. Abdo et al** ,Fermi Large Area Telescope Bright Gamma-ray Source List , *2009 Astrophysical Journal Volume 183 Issue 46*, https://iopscience.iop.org/article/10.1088/0067-0049/183/1/46

[30] **M. Ackermann et al**, THE FIRST FERMI-LAT GAMMA-RAY BURST CATALOG , *2013 Astrophysical Journal Volume 209 Issue 11* https://iopscience.iop.org/article/10.1088/0067-0049/209/1/11/meta

[31] **W.B. Atwood et al**,The Large Area Telescope on the Fermi Gamma-Ray Space Telescope Mission , *2009 Astrophyical Journal Volume 697 Issue 2* https:

//ui.adsabs.harvard.edu/abs/2009ApJ...697.1071A/abstract

[32] **NASA/DOE/Fermi LAT Collaboration** https://svs.gsfc.nasa.gov/11342

[33] **Abeysekara et al**,Observation of the Crab Nebula with the HAWC Gamma-Ray Observatory , *2017 Astrophyical Journal Volume 843 Issue 1* https://iopscience.iop.org/article/10.3847/1538-4357/aa7555/meta

[34] **Tyce DeYoung**,The HAWC observatory , *2012 Nuclear Instruments and Methods in Physics Research Section A: Accelerators, Spectrometers, Detectors and Associated Equipment Volume 692* https://www.sciencedirect.com/science/article/abs/pii/S0168900212000666?casatoken=UZ4xIbPPpMAAAAA:zVzcZpkZ-7RMY7OVPJC-iRzASukBR1-i4ewJ73m9Eo29IcbkclNhSoqkner94Maw9n7PyfIZg

[35] HAWC The High-Altitude Water Cherenkov Gamma-Ray Observatory , *visited on 01.03.2022* https://www.hawc-observatory.org/observatory/sensi.php

[36] **Ibrahim Torres, Alberto Carraminana, Ruben Alfaro, Arturo Iriarte**, Deployment of the HAWC gamma-ray observatory in Sierra Negra, Mexico , *2013 33rd international cosmic ray Conference* https://www.researchgate.net/publication/257246847TheHAWCGamma-RayObservatoryDesignCalibrationandOperation

[37] **Stefan Funk, James Anthony Hinton**, Monte-Carlo studies of the angular resolution of a future Cherenkov gamma-ray telescope , *2009* https://www.researchgate.net/publication/23786947Monte-CarlostudiesoftheangularresolutionofafutureCherenkovgamma-raytelescope

[38] Documentation of the python package gammapy v.0.18.2 , *visited on 01.08.22* https://docs.gammapy.org/0.19/getting-started/index.html

[39] **Ti-Pei Li, Yu-Qian Ma**, ANALYSIS METHODS FOR RESULTS IN GAMMA-RAY ASTRONOMY , *1983 Astrophyical Journal Volume 272* https://articles.adsabs.harvard.edu/pdf/1983ApJ...272..317L

[40] Documentation of the python package fermipy v.1.0.1 , *visited on 01.12.22* https://fermipy.readthedocs.io/en/latest/index.html

[41] **Matthew Wood**, Fermipy Documentation Release v1.0.1+dirty , *1921* https://fermipy.readthedocs.io//downloads/en/stable/pdf/

[42] **Abeysekara et. al.**, The 2HWC HAWC Observatory Gamma-Ray Catalog , *2017, The Astrophysical Journal, Volume 843* https://ui.adsabs.harvard.edu/abs/2017ApJ...843...40A/abstract

[43] **R.D. Parsonsa, J.A. Hinton**, A Monte Carlo Template based analysis for Air-Cherenkov Arrays , *2014, Astroparticle Physics Volume 56* https://arxiv.org/abs/1403.2993

[44] **M. Breuhaus, B. Reville, J. A. Hinton**, A pulsar wind nebula origin of the LHAASO-detected UHE γ-ray sources , *2021* https://arxiv.org/pdf/2109.05296.pdf

[45] **Breuhaus et al.**, Ultra-high energy Inverse Compton emission from Galactic electron accelerators, *2021, The Astrophysical Journal Letters, Volume 908* https://ui.adsabs.harvard.edu/abs/2021ApJ...908L..49B/abstract

[46] **Principe et al.**, Energy dependent morphology of the pulsar wind nebula HESS J1825-137 with Fermi-LAT , *2020, Astronomy & Astrophysics Volume 640* https://www.aanda.org/articles/aa/fullhtml/2020/08/aa38375-20/aa38375-20.html

[47] **Aharonian et al.**, Energy dependent γ-ray morphology in the pulsar wind nebula HESS J1825-137 , *2006, Astronomy & Astrophysics Volume 460* https://arxiv.org/pdf/astro-ph/0607548.pdf

[48] **P. K. H. Yeung, D. Horns**, The Energy-dependent γ-Ray Morphology of the Crab Nebula Observed with the Fermi Large Area Telescope , *2019, The Astrophysical Journal, Volume 875* https://iopscience.iop.org/article/10.3847/1538-4357/ab107a

[49] **Fang-Wu Lu, Quan-Gui Gao, Li Zhang**, Energy-dependent nebula extent and spatially resolved spectra of the pulsar wind nebula 3C 58 , *2020, Monthly Notices of the Royal Astronomical Society, Volume 498* https://academic.oup.com/mnras/article/

498/2/1911/5906317?login=true

[50] **Grodin et al.**, THE VELA-X PULSAR WIND NEBULA REVISITED WITH FOUR YEARS OF FERMI LARGE AREA TELESCOPE OBSERVATIONS, *2013, The Astrophysical Journal, Volume 774* https://iopscience.iop.org/article/10.1088/0004-637X/774/2/110/meta

[51] **H.E.S.S. Collaboration**, Acceleration of Petaelectronvolt protons in the Galactic Centre , *2016, Nature Volume 531* https://arxiv.org/abs/1603.07730

[52] **Camilo et al.**, Radio Detection of PSR J1813-1749 in HESS J1813-178: The Most Scattered Pulsar Known , *2021, The Astrophysical Journal, Volume 917* https://ui.adsabs.harvard.edu/abs/2021ApJ...917...67C/abstract

[53] **J. P. Halpern, E. V. Gotthelf, and F. Camilo**, Spin-down Measurement of PSR J1813-1749: The Energetic Pulsar Powering HESS J1813-178, *2012, The Astrophysical Journal Letters, Volume 753* https://ui.adsabs.harvard.edu/abs/2012ApJ...753L..14H/abstract

[54] **Messineo et al.**, Massive Stars in the Cl 1813-178 Cluster: An Episode Of Massive Star Formation in the W33 Complex, *2011, The Astrophysical Journal, Volume 733* https://ui.adsabs.harvard.edu/abs/2011ApJ...733...41M/abstract

[55] **Messineo et al.**, Discovery of a Young Massive Stellar Cluster near HESS J1813-178, *2008, The Astrophysical Journal Letters, Volume 683* https://ui.adsabs.harvard.edu/abs/2008ApJ...683L.155M/abstract

[56] **S. A. Dzib, L. F. Rodriguez**, Radio Proper Motions of the Energetic Pulsar PSR J18131749, *2021, The Astrophysical Journal, Volume 923* https://arxiv.org/pdf/2110.09727.pdf

[57] **Ahronian et al.**, Discovery of two candidate pulsar wind nebulae in very-high-energy gamma rays , *2007, Astronomy and Astrophysics, Volume 472* https://arxiv.org/pdf/0705.1605.pdf

[58] **O. Kargaltsev, G. G. Pavlov**, X-RAY EMISSION FROM PSR J1809-1917 AND ITS PULSAR WIND NEBULA, POSSIBLY ASSOCIATED WITH THE TeV GAMMA-RAY SOURCE HESS J1809-193 , *2007, The Astrophysical Journal, Volume 670*

https://iopscience.iop.org/article/10.1086/521814/pdf

[59] **Anada et al.**, X-Ray Studies of HESS J1809−193 with Suzaku, *2010, Publications of the Astronomical Society of Japan Volume 62* https://ui.adsabs.harvard.edu/abs/2010PASJ...62..179A/abstract

[60] **Abeysekara et al.**, Extended gamma-ray sources around pulsars constrain the origin of the positron flux at Earth, *2017, Science, Volume 358* https://ui.adsabs.harvard.edu/abs/2017Sci...358..911A/abstract

[61] **NASA**, Fermi LAT Performance, visited at 02.03.2022 https://www.slac.stanford.edu/exp/glast/groups/canda/latPerformance.htm

[62] **J. Zorn**, Cherenkov Camera and Analysis Development for Highest-Energy Gamma-Ray Astronomy https://www.imprs-hd.mpg.de/408842/thesisZorn.pdf

Acknowledgements

Finally, I would like to thank everyone who supported me during this thesis. In particular, I would like to thank:

- Prof. Dr Stefan Funk for giving me the opportunity to work on a very interesting topic and the helpful input on the various occasions.
- Vikas Joshi for the support and good advice throughout the thesis and also for proof-reading this document.
- Alison Mitchell for always providing me with helpful comments and explanations.
- Tim Unbehaun for his support and patients whenever I had technical problems.
- The whole Gamma-ray group for being such a great team

Statement of Authorship

I hereby declare that I have written this thesis without outside help and without using any sources other than those indicated. All thoughts or quotations which were inferred from these sources are clearly marked as such.

Erlangen den 01.04.22

Tina Wach